FINAL SCIENTIFIC/TECHNICAL REPORT DOE AWARD NO. DE-SC0011348, STTR PHASE II

Project Title:	**A Hybrid HTS/LTS Superconductor Design for High-Field Accelerator Magnets**
Report Date:	08/13/2018
Report Number:	DOE-PBL-20180704
Company Name:	Particle Beam Lasers, Inc.
Principal Investigator:	Ramesh Gupta

Purpose of Research, Research Carried Out, and Research Findings:

Fabricating and testing a proof-of-principle hybrid HTS/LTS common-coil dipole, and improving the field homogeneity in magnets of ReBCO tape, have advanced technology for accelerator magnets. High-strength ReBCO tape with a Hastelloy substrate has long been the preferred approach for high field magnets, because it can withstand high stresses, but was deemed impractical, primarily because its propensity to magnetize wreaks havoc with field homogeneity. The technique developed during our Phase II project shows great promise in reducing magnetization to an acceptable level. As a result, very high field magnets made with ReBCO HTS tape now may become viable for future circular colliders.

We demonstrated a proof-of-principle HTS/LTS hybrid magnet. Facilitating accomplishment of this ambitious task was a magnet unique to BNL that, without the prohibitive cost of disassembly and reassembly, can accommodate coils of HTS for testing in a background field as high as 10 T. The design techniques demonstrated may reduce the quantity, and hence the cost, of expensive HTS by a factor of two or more.

PBL, BNL and e2P developed a preliminary engineering design for an economical 20 T dipole magnet amenable to mass production. The design and technology are likely to be useful in other areas as well; PBL is soliciting interest by other companies. The work performed has led to the award of US Patent number 9793036: “A Low Temperature Superconductor and Aligned High Temperature Superconductor Magnetic Dipole System and Method for Producing High Magnetic Fields”.

Potential Applications of the Research:

Hybrid HTS/LTS magnets are uniquely suited for economical, reliable high-field magnets for multi-billion-dollar colliding-beam particle accelerators. To further their development, this STTR pioneered methods for improving field quality and supporting the superconductor against the huge Lorentz forces experienced in high-field magnets. The technology developed may benefit commercial superconducting magnets as well, in applications that include nuclear magnetic resonance, magnetic resonance imaging, proton and ion-beam therapy, wind power, and superconducting magnet energy storage.

FINAL SCIENTIFIC/TECHNICAL REPORT DOE AWARD NO. DE-SC0011348, SBIR PHASE II

Recipient:	**Particle Beam Lasers, Inc.** **18925 Dearborn Street** **Northridge, CA 91324-2807**
Sponsoring Program Office:	**Division of High Energy Physics** **Office of Science** **U.S. Department of Energy**
Project Title:	**A Hybrid HTS/LTS Superconductor Design for High-Field Accelerator Magnets**
Principal Investigator:	**Ramesh Gupta, BNL**
Team Members:	Michael Anerella, BNL John Cozzolino, BNL Piyush Joshi, BNL Shresht Joshi, BNL James Kolonko, PBL Delbert Larson, PBL Chris Rey, e2P William Sampson, BNL Ronald M. Scanlan, PBL Jesse Schmalzle, BNL Robert Weggel, PBL Erich Willen, PBL

This material is based upon work supported by the U.S. Department of Energy, Office of Science, Office of High Energy Physics under Award Number DE-SC0011348.

SECTION ONE. OVERVIEW OF WORK COMPLETED

SIGNIFICANCE, BACKGROUND INFORMATION, AND TECHNICAL APPROACH

The 2014 Particle Physics Project Prioritization Panel (P5) vision document [1] addressed pressing scientific questions and made dozens of recommendations to the U.S. Department of Energy. Recommendation #24 was: "*Participate in global conceptual design studies and critical path R&D for future very high-energy proton-proton colliders. Continue to play a leadership role in superconducting magnet technology focused on the dual goals of increasing performance and decreasing costs.*" This STTR developed new technologies for high-field superconducting magnets for high-energy proton colliders.

Proposed high-energy accelerators such as CERN's Future Circular Collider (FCC) [2] and China's CEPC/SppC [3] envision dipole magnets with central fields as high as 20 T. The maximum field on the conductor will be even higher (maybe by 10% or so) to allow for a safety margin for operation and because the maximum coil field is higher than the central field. Adequate current density at such fields requires high-temperature superconductor (HTS) such as Bi2212 or ReBCO (rare-earth barium copper oxide—YBCO, if the rare earth is yttrium).

HTS is expensive and is likely to remain so. A hybrid design that uses LTS as well as HTS reduces the cost of magnets by employing HTS only in the regions that require it—where the field is greater than ~15 T at 4 K (see Fig. 1). This STTR demonstrated the first significant test of an HTS/LTS hybrid dipole. It built and tested small HTS dipole coils and integrated them into a dipole test facility unique to BNL: a Nb_3Sn common-coil dipole ("DCC017") [4] of high field (10 T) and large opening (31 mm horizontal by 338 mm vertical) that requires no disassembly and reassembly to accommodate test coils. This capability permitted tests sufficiently economical for an STTR to demonstrate the basic principles of HTS/LTS hybrid magnet fabrication and operation. Other equipment facilitating the STTR included a state-of-the-art quench protection system developed in previous SBIR/STTRs by the PBL/BNL team.

This STTR advances high field magnet technology by mitigating conductor magnetization issues, withstanding high stresses, and reducing magnet cost by reducing the amount of HTS required.

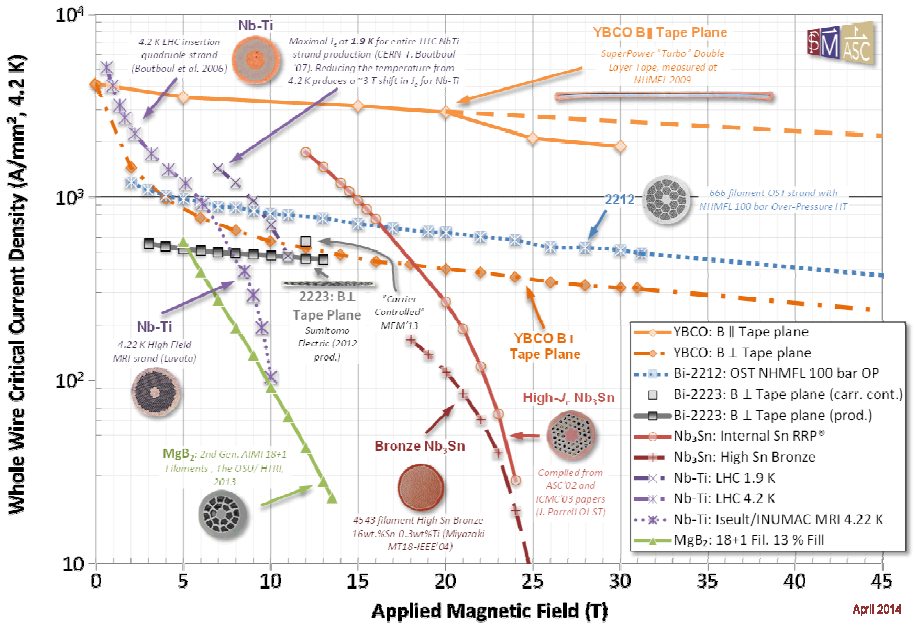

Fig. 1. Engineering current density for HTS (YBCO tape and Bi2212 wire) compared to other high field superconductors, showing the necessity for HTS at the highest fields. Data compiled by P. Lee, NHMFL.

ANTICIPATED PUBLIC BENEFIT

High-temperature superconductor magnet technology is crucial for the magnets of unprecedented field and operating temperature for fundamental research beyond the discovery of Higgs bosons. Commercial spin-offs—in areas not only of research but also medical, energy and national security—are likely to follow the development of this technology, just as the development of NMR and MRI magnets followed LTS magnet technology developed for previous generations of HEP accelerator magnets. Because HTS is costly and likely to remain so, commercial viability of the magnets requires a hybrid design, using HTS only where the field is too high for LTS. The conductor and coil-performance tests of this STTR should encourage conductor manufacturers to improve their product to better meet the needs of the magnet community.

WORK PERFORMED ON THE PHASE II TECHNICAL OBJECTIVES

("Objectives 1 through 6 contain proprietary information, trade secrets or commercial information that is privileged or confidential and exempt from public disclosure.")

The ultimate technical objective of this proposal was to develop technology for a 20 T HTS/LTS hybrid dipole, demonstrating the key features of the technology in a proof-of-principle design. Its success should attract funding to carry out further R&D, to build a prototype magnet, and eventually to commercialize full-length dipoles. Notably, our design exploits the superior magnetic and mechanical properties of ReBCO tapes while practically eliminating the field inhomogeneity from magnetization typically incurred with their use. The specific objectives achieved by this STTR are outlined below.

Objective 1: Technique to Reduce Field Errors Due to Magnetization in HTS Tape

Magnetization of superconductors is caused by currents induced by Lentz's Law to oppose the change in field, shielding the interior of the conductor during up-ramps, and trapping field internally during down-ramps. The magnitude of the magnetization is proportional to the product of the density of these induced currents times their separation. For ReBCO tape, the separation distance is less than 1 μm within the thickness of the superconducting film but can be a centimeter or so across the breadth of the tape, an aspect ratio of four orders of magnitude.

Only the field component that is out of the plane of the tape can induce currents separated by millimeters, not microns. Logic suggests that to eliminate conductor magnetization one should eliminate its activating agent, this field component. It is infeasible to force the ambient field to align favorably throughout more than a fraction of a magnet; this analysis proposes instead to align the HTS tapes to conform to the ambient field.

A convenient model of the magnetizability of the superconductor is orthotropic permeability, with the component that is out of the plane of the tape having sub-unity permeability. The model does not address hysteresis, but it can estimate the magnetic field inhomogeneity from magnetization and predict its revolutionary reduction from aligning the tape with the ambient field. The analysis argues energetically and persuasively for tape alignment, predicting that tilting conductor uniformly throughout a conductor block, even if of considerable winding depth, can nearly eliminate field-quality degradation. Tape splaying and/or cupping (like the slats on a venetian blind) can further improve alignment, and may be worth the trouble if the field uniformity needs to be especially good, or to persist over a range of fields.

Measurements by the BNL Superconducting Magnet Division for this STTR confirmed that the perturbations to the central field of a magnet of ReBCO tape are less—by a factor of two, for their magnet geometry—when the ambient field direction is more nearly in the plane of the tape than perpendicular to it. The analysis below studies the benefits to be had—especially the reduction in nuisance fields from conductor magnetization—that may accrue from orienting tape favorably relative to the ambient field. The illustrative magnets are dipoles, modeled in 2D, to generate 20 T, of which approximately 40% is from ReBCO tape 12 mm wide.

To investigate the benefits of tape tilting, the analysis first computes the field uniformity of an illustrative dipole magnet with conductor cross sections as in Fig. 2a. Its nine conductor blocks are in three sets of three, the inner of HTS, the intermediate of Nb_3Sn, and the outer of NbTi, except for its outboard block, which needs to be Nb_3Sn because of the high horizontal (x) component of field. All current densities are 600 A/mm^2—ambitous, but not unprecedented—with the HTS current density tweaked slightly if necessary to maintain the central field of 20 T.

Were the field to come from transport current only, unaltered by conductor magnetization, the field quality would be 12th order; in the power series expansion that describes its field inhomogeneity, the first term not annullled is $c_{12}\ r^{12} \cos(12\ \theta)$; the contour pattern of Fig. 2c displays the characteristic six spikes and six lobes per quadrant. Each set individually is 12th order, to reveal more clearly any field perturbations introduced by magnetization of the HTS tape. The region of field homogeneity of one part in 10^4 (navy contours) reaches 15.1 mm along the horizontal axis and approximately 10% greater along the vertical axis.

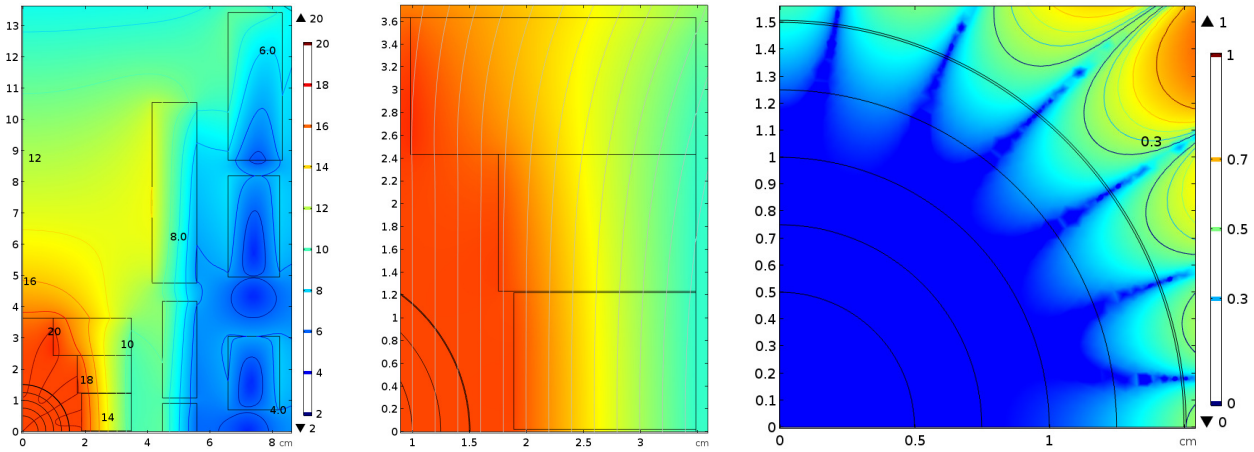

Fig. 2a-c: Illustrative 2D dipole magnet with field homogeneity of 12th order. Left: Field magnitude (color & contours). Center: Streamlines. Right: Logarithmic inhomogeneity ΔB_y: $4+\log_{10}(\Delta B_y/B_0)$, where $\Delta B_y \equiv |B_y - B_0|$. Successive contours, in parts in 10^4, are [1 (navy), 2 (cyan), 3.2 (green), 5 (orange), and 10 (maroon). Radius r_1 to nearest violation of $1\text{x}10^{-4}$ homogeneity criterion is 15.1 mm.

The model of sub-unity out-of-plane permeability μ_x predicts severe degradation of field homogeneity if tape is not tilted. Permeability that is only 10% less than unity shrinks by 24% the radius r_1 to the nearest point with field nonuniformity in excess of 1 part in 10^4 (Fig. 3a); for $\mu_x = 50\%$ the contour shrinkage is a factor of nearly two. For $\mu_x = 10\%$ the field homogeneity fails the $1\text{x}10^{-4}$ criterion at $r_1 = 2.1$ mm, a mere one-seventh of the original radius. The magnetization (Fig. 3b) reaches 10.4 kA/mm, which translates to a field of 13 T.

Comparing the streamlines of Fig. 3b—all quasi-parallel to the y axis—with those of Fig. 2b reveals the extent to which magnetization has altered the field distribution of the magnet, especially internally. A prediction of the orthotropic permeability model is that for $\mu_x = 0.1$ magnetization has so altered the field from the HTS magnet as to require an 11% increase in its current to retain its field contribution of 8 T.

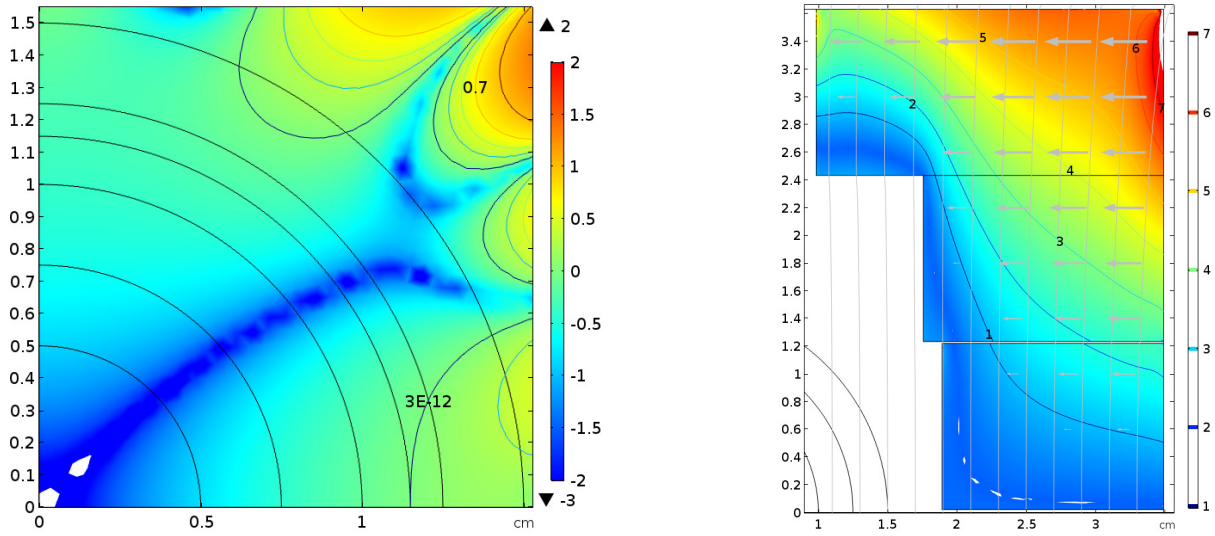

Fig. 3a&b. Untilted tape with sub-unity out-of-plane permeability μ_x. Left: $\mu_x = 90\%$; $\log_{10}(\Delta B_y/B_0)$, in parts in 10^4 (color & contours); minimum radius r_1 to $\Delta B/B_0 = 1\text{x}10^{-4}$ is 11.5 mm. Right: $\mu_x = 10\%$; field direction (streamlines), magnetization direction (arrows) and magnitude M (color & contours); maximum is 10.4 kA/mm.

Magnetization can be reduced, and field homogeneity consequently better preserved, if tape is tilted optimally. To determine the optimum tilt, a COMSOL FEM program, augmented by its Optimization Module, adjusts tape tilt angles to minimize the integral, inside a circle of radius R, of the product of $(\Delta B_y/B_0)^2$ and a weighting factor $w(r,\theta) \equiv w(x,y) \equiv w(u,v)$, where $u \equiv x/R$ and $v \equiv y/R$. Judicious choice of R and w minimizes the weighted field inhomogeneity throughout the region of interest, with the goal of maximizing the radius r_1 of the circle that fits inside all lobes of the homogeneity-criterion contour; when so maximized, the circle usually grazes more than one lobe. Symmetric weighting factors such as $[1 - (r/R)^n]$ may suffice, but better may be $(1 - u^n)$ or $(1 - v^n)$, whose penalty factor remains strong along one axis but weakens to zero a distance R along the other. Intermediate is a function such as $(1+u^2+3v^2)^{-1}$ which, at counterclockwise 15° increments along the circle $r = R$, evaluates to [0.500, 0.469, 0.400, 0.333, 0.286, 0.259, 0.250].

Tilting the tape uniformly in each block can go far toward improving field quality. Figures 4a&b plot the field inhomogeneity $\Delta B/B_0$ and magnetization magnitude M predicted for a 10% out-of-plane permeability (μ_x = 0.1 in the coordinate system of the tilted tape). Tilt slopes (rise ÷ hypotenuse) in the HTS blocks are 0.0152, 0.0896 and 0.1258, inboard to outboard. The homogeneity criterion of $1\text{x}10^{-4}$ is not violated until a radius of 11.5 mm, five times larger than with no tilt. The magnetization is reduced only somewhat in magnitude, from 10.4 kA/mm^2 to 8.1 kA/mm^2, but it now is balanced, with almost identical positive and negative maxima. The component M_x ranges from −8.00 kA/mm to +7.97 kA/mm; the range for the component M_y (≡ M times the sin of the tilt angle) is ±1.01 kA/mm. The optimal tilt approximates the average slope $\tan^{-1}\langle B_x/B_y\rangle \equiv \sin^{-1}\langle B_x/B\rangle$ of the field streamlines; likely somewhat better, to avoid overweighting regions in which both field components are small, is $\tan^{-1}(\langle B_x\rangle/\langle B_y\rangle) \equiv \sin^{-1}(\langle B_x\rangle/\langle B\rangle)$, the ratio of averages, rather than the average of the ratio. For the three HTS blocks of Fig. 4, $\langle B_x\rangle/\langle B\rangle$ = 0.0176, 0.0939, and 0.1382, respectively, compared to which the optimum tilt slopes are 86%, 95% and 91%. Figure 4c plots the magnetization for μ_x. = 1%—nearly complete rejection of flux penetration. M becomes very high—up to 27 kA/mm—but it is localized to the inner and outer surfaces and balanced so well that $\Delta B_y/B_0$ meets the $1\text{x}10^{-4}$ criterion to a radius of 11.1 mm, only 4% less than for μ_x. =10%.

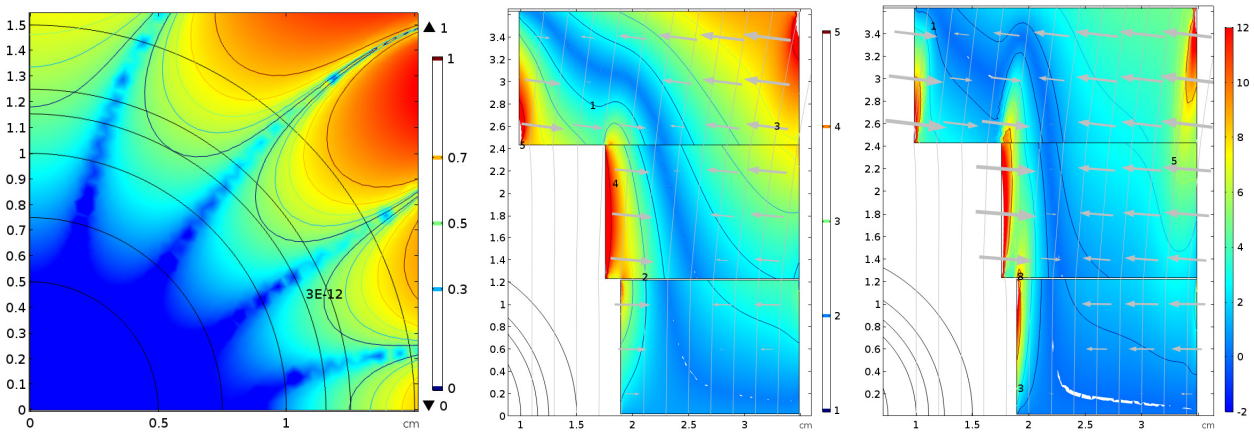

Fig. 4a-c. $\Delta B_y/B_0$ and magnetization M of Fig. 2a magnet with tilted tape with out-of-plane permeability μ_x. Left: μ_x. =10%; $\Delta B_y/B_0$ (color & contours) reaches $1\text{x}10^{-4}$ (navy contour) at radius of 11.5 mm at the two lobes near one o'clock. Center (μ_x = 10%) and Right (μ_x = 1%): Field streamlines and M [kA/mm] direction (arrows) and magnitude (color & contours), evidencing excellence of balance.

Figure 5 graphs, as a function of the out-of-plane permeability, the predicted ability of tape tilting to maintain field homogeneity in the illustrative ReBCO magnet of Fig. 2a. Comparison of the red curve with the black one reveals that the predicted improvement is phenomenal, especially when the out-of-plane permeability is small. The blue curve suggests why the field homogeneity with untilted tape degrades so badly with increasing magnetizability: the central field magnitude itself is affected so greatly as to require a major increase in transport current to maintain the central field.

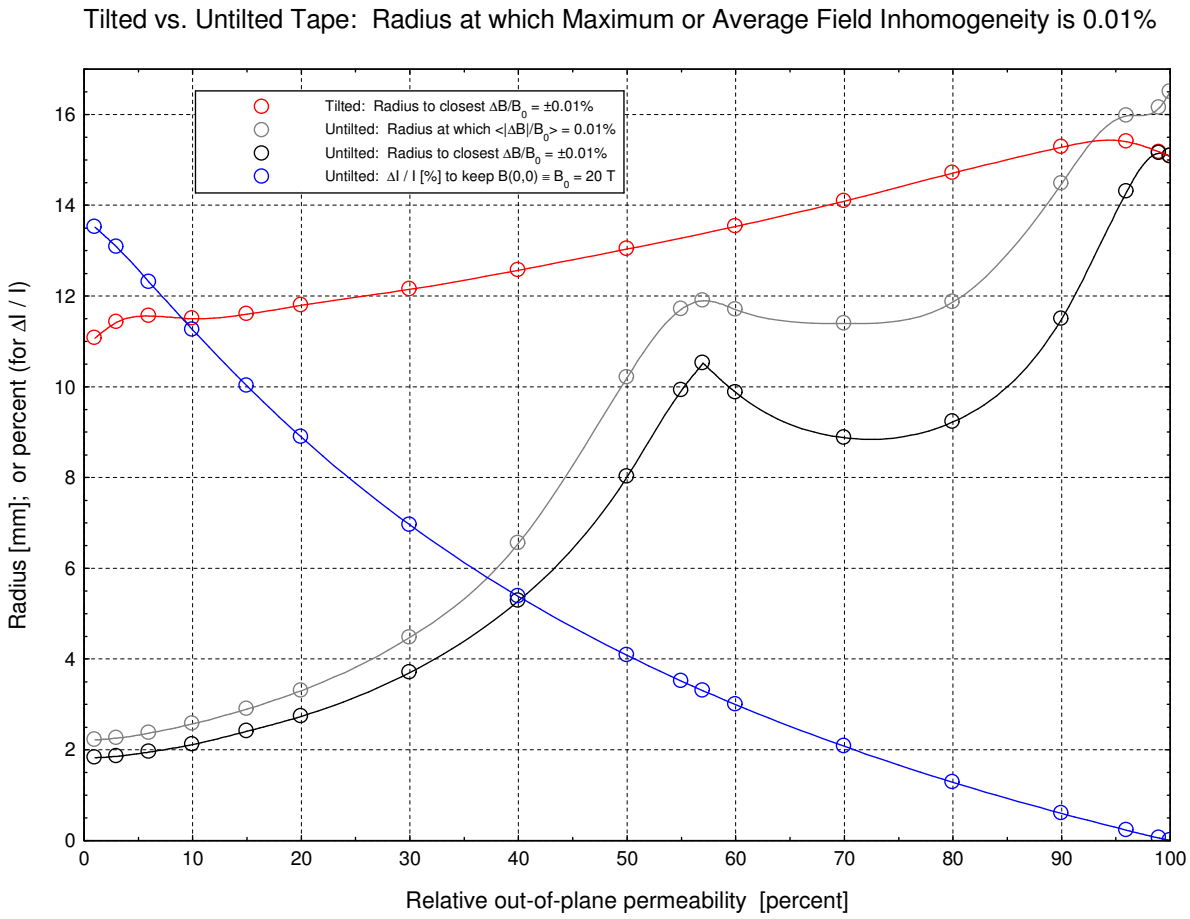

Fig. 5. Predicted ability of tape tilting to maintain field homogeneity $\Delta B_y/B_0$ in the illustrative ReBCO magnet of Fig. 2a, compared with loss of field homogeneity if tape is not tilted.

Another analysis considered HTS conductor blocks that are parallelograms, as created by sets of tilted tapes, every tape in each set having its lower edge at the same y coordinate. Figure 6a diagrams the cross section of conductor blocks—outer rectangles of low-temperature superconductor and inner parallelograms of ReBCO tape 12 mm wide. Streamlines show the field direction; color & contours, its magnitude from transport current alone (zero magnetization). Figure 6b plots the streamlines at a larger scale and, in color and contours, also their slope B_x/B_0. Figure 6c reveals the field homogeneity to be nominally of 10^{th} order.

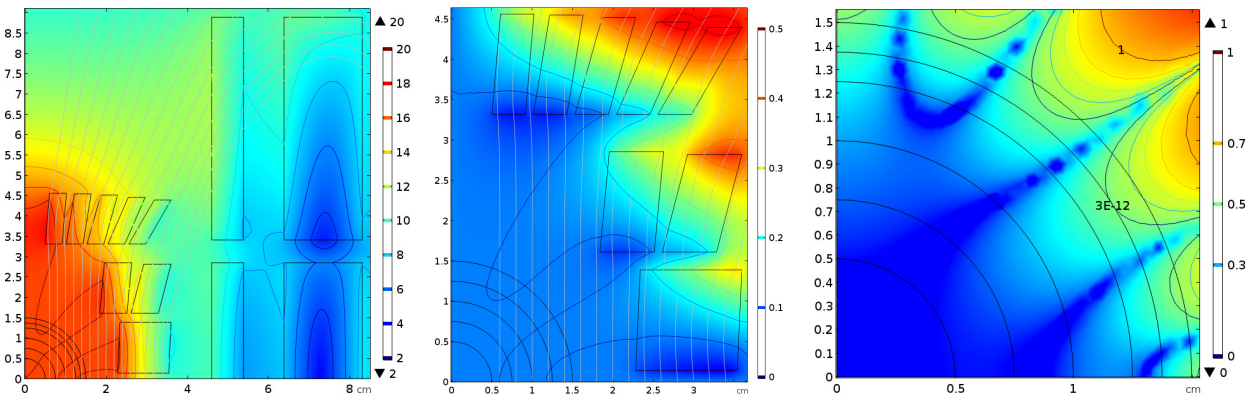

Fig. 6a-c. Illustrative 20 T magnet with eight parallelograms of tilted HTS tape. Left: Magnetic field direction (streamlines) and magnitude (color & contours) from transport current alone (zero magnetization). Center: Field direction (streamlines) and slope B_x/B_0 [color & contours]. Right: Field homogeneity is nominally 10th order, with homogeneity criterion (navy contour) reached at r_1 = 13.8 mm.

Figure 7 plots the field homogeneity and streamlines and the magnetization direction and magnitude for an out-of-plane permeability of 50%. Maximization of the region of field uniformity employed a weighting-factor radius R = 15 mm and a weighting factor $w = (1 - v^6)$, where $v \equiv y/R$.

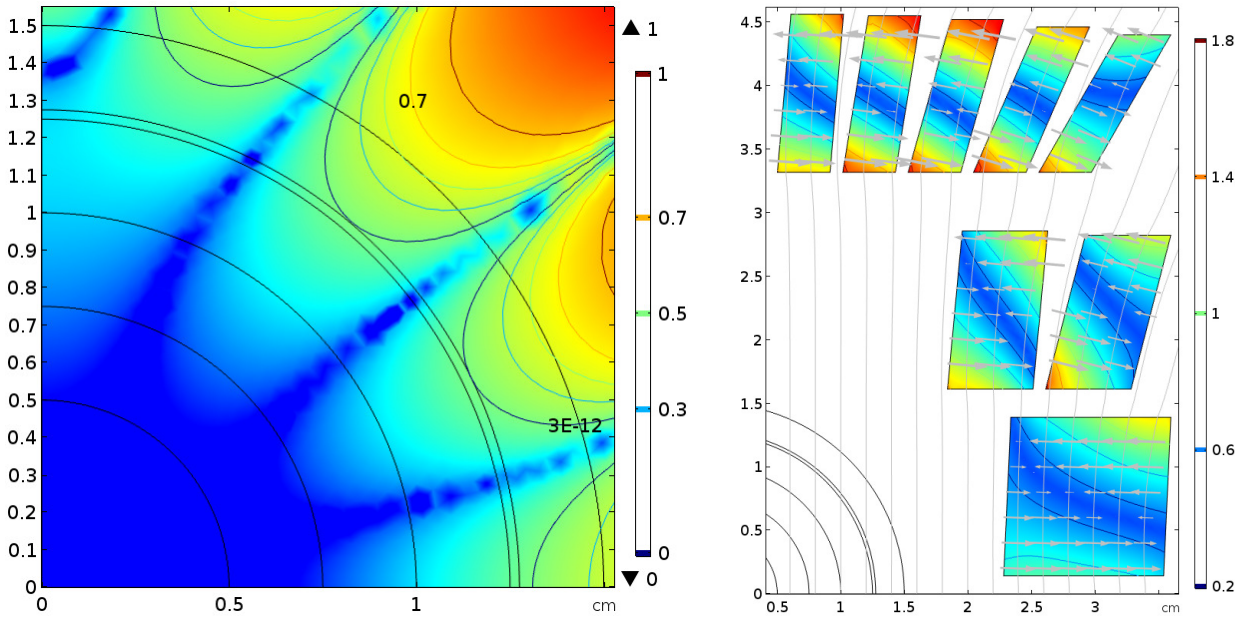

Fig. 7a&b. Figure 6a magnet with out-of-plane permeability 50%. Left: Field homogeneity (color & contours); radius r_1 to nearest 1x10^{-4} contour is 12.8 mm. Right: Field direction (streamlines) and magnetization direction (arrows) and magnitude M (color & contours); maximum M = 2.80 kA/mm; M_x ranges from −2.21 kA/mm to +2.08 kA/mm; M_y, from −0.69 kA/mm to +0.52 kA/mm.

Throughout a conductor block the field slope s ≡ B_x/B_0 may vary significantly with x, the distance from the vertical axis, as seen from the splay of the streamlines in Fig. 6b. To bring the tape and ambient-field slopes inot better agreement, one can consider augmenting the tilt from tape to tape by a uniform splay ds/dx Δx, where Δx is the distance between consecutive layers of tape. Similarly, one can consider adding a uniform (parabolic) tape curvature ds/dy to follow the

streamline curvature, cupping each tape like the slat of a metal venetian blind, to mimic the direction of ambient field along the complete width of the tape. Analysis of magnets with this degree of complexity is ongoing, with conclusions only tentative so far.

So far, predictions unexpectedly suggest that splaying and cupping tape are of little benefit. Figure 8a predicts that for the Fig. 6a magnet with $\mu_x = 50\%$ the region of field uniformity grows by only several percent—implausibly little. However, Figure 8b predicts a reduction in magnetization that may be very significant, perhaps maintaining the field uniformity over a much wider range of permeability, and hence magnetic field. Not only is the maximum magnetization less by a factor of two, it is even more balanced than before, with consecutive corners of each parallelogram alternating in sign.

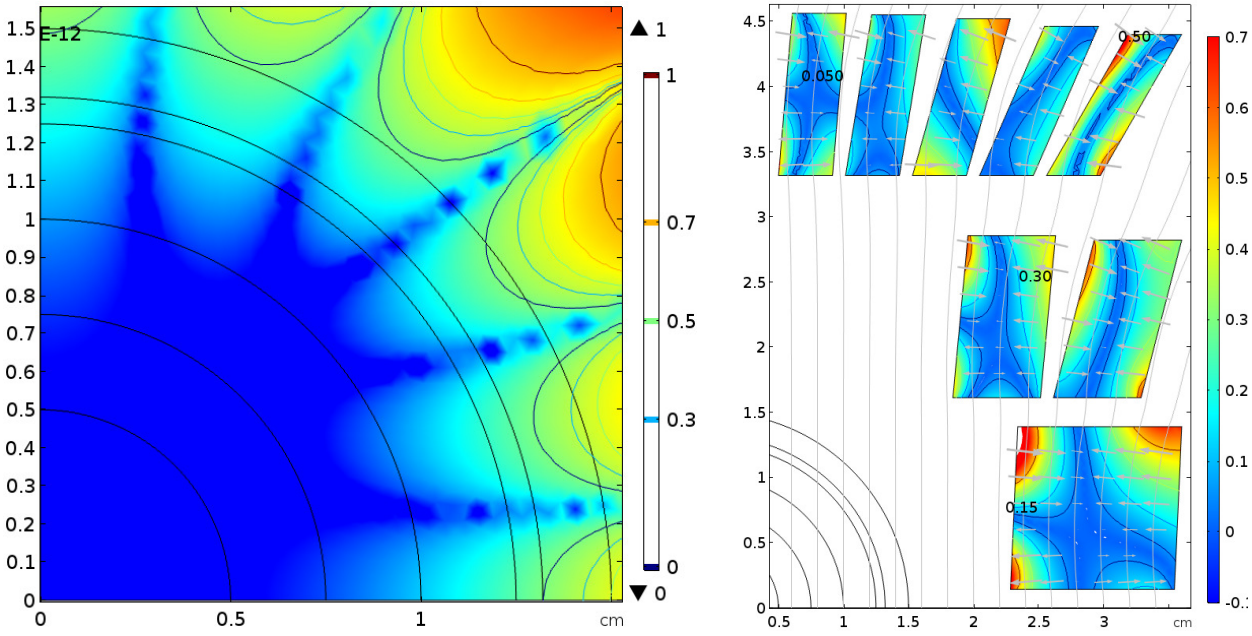

Fig. 8a&b. 8 HTS blocks, tilted, splayed & cupped; $\mu_x = 50\%$. Left: Field homogeneity (color and contours); weighting factor = $1 - v^2$; $\Delta B/B_0 = 1\text{x}10^{-4}$ at $x = r_1 = 13.20$ mm. Right: Field direction (streamlines) and magnetization magnitude (color & contours) and direction (arrows); maximum magnetization = 1.15 kA/mm.

Magnetization of Racetrack Magnets of ReBCO Tape

The following section documents analyses of the magnetization of ReBCO-tape in racetrack magnets consisting of a pair of racetrack coils of conductor 12 mm wide, each coil with a winding depth of ~12 mm (35 turns, each 0.34 mm thick), end arcs of inner radius 112 mm and outer radius 124 mm, and straight legs 305 mm long. Figure 9 shows a quadrant of one of the coils, meshed especially finely near the region of greatest interest—in and near the mid-region of its leg. As drawn, the leftmost face, part of the symmetry plane $x = 0$, ranges from 106 mm to 130 mm in y, and zero to 18 mm in z. The mesh is illustrative only; the actual mesh typically is four or five times finer in each direction.

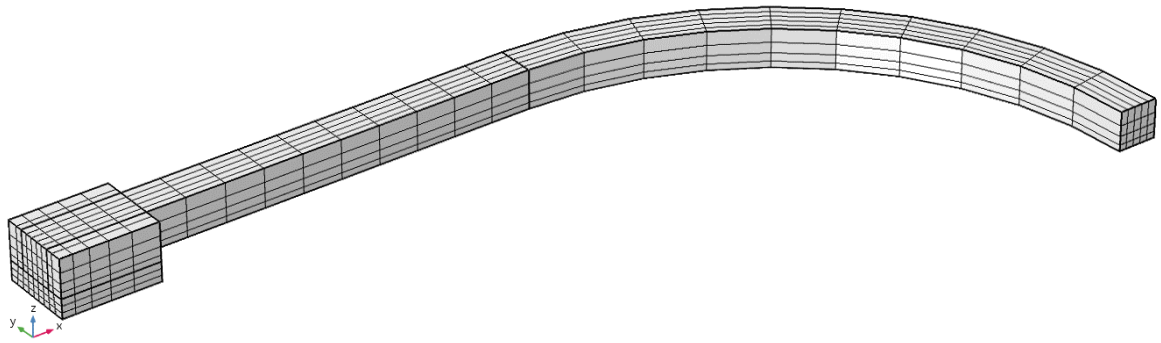

Fig. 9: Quadrant [x>0, y>0] of racetrack coil of ReBCO tape 12 mm wide (vertical, z, direction) and winding depth ~12 mm. Inner radius of the arc is 112 mm; outer radius is 124 mm. The actual mesh is much finer in all directions.

The magnet configuration known as "common-coil" employs two such coils, as in a Helmholtz pair, with a midplane gap between the two members; if oriented as in Fig. 9, one coil is directly above the other. However, unlike in a Helmholtz pair, the coils are energized in opposition, like diametrically-opposite coils of a quadrupole. The field throughout the midplane of the gap is purely in that plane. In a common-coil magnet with two racetracks as described in the preceding paragraph, the field along the line $x = 0$ peaks near the coil mid-build of 118 mm, with a value of 1.145 mT/A when the inter-coil gap Δz is 12 mm between the upper face of the lower coil and the lower face of the upper coil. If the midplane gap is reduced to 3 mm, so that the magnet will fit in the 31 mm gap of BNL's Nb_3Sn racetrack dipole DCC017, the coil constant rises 53% to 1.75 mT/A. This geometry investigates magnetization of the ReBCO tape with the component of field perpendicular to the surface of the tape typically larger than the in-plane component. **Confusion alert**!: Mathematicians define the direction of a plane by its normal vector, the cross product of any non-co-linear vectors lying in the plane of the tape; according to *this* definition, the field direction described above typically has its largest field component parallel, not perpendicular, to the tape.

An alternative conductor configuration, to investigate the magnetization with the perpendicular field component typically smaller than the in-plane component, positions the adjacent conductors side by side, sharing a common plane, like the outspread wings of a butterfly. Throughout the vertical symmetry plane of the "butterfly body"—midway between the horizontally adjacent conductors—the field has no y component. If the gap Δy is the same 12 mm as in the common-coil dipole above, the field is nearly the same as before (less by 1.4%), confirming that near the mid-length of the adjacent straight legs, almost all of the field comes from the nearby legs, very little from the return paths.

Bill Sampson, Ramesh Gupta and other personnel of BNL's Superconducting Magnet Division measured the magnetic field from magnets with the racetrack coils in both configurations—common coil and butterfly. Measurements were by a Hall probe centered where two of the magnet's planes of symmetry intersect near the letter "*z*" in Fig. 9. Usually the magnet was immersed in liquid nitrogen; for a few measurements the common-coil magnet was at 4 K. Figure 10a graphs the field versus time for an energization sequence of the common-coil at 77 K. Each upward ramp of current was followed by a holding period of five to six minutes to allow the field to stabilize. Figure 10b plots the measured field immediately before beginning each down-ramp of current to zero.

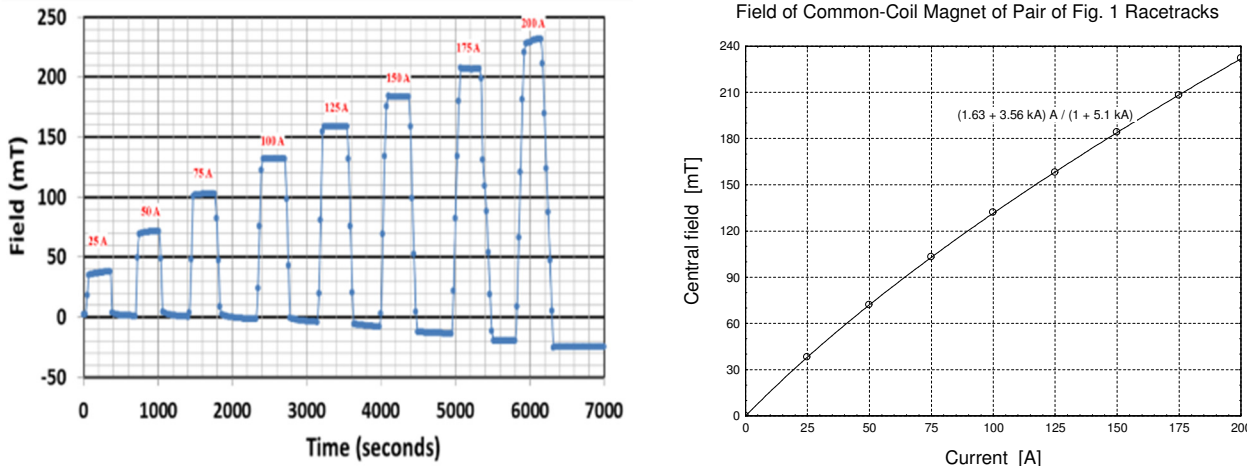

Fig. 10a&b. Common-coil magnet of pair of Fig. 9 racetrack coils. Left: Energization sequence. Right: Field at end of each current flat-top.

Table I summarizes the Fig. 10 measurements of field at the end of each constant-current holding period—B_+ immediately before each down-ramp, B_- immediately before each up-ramp from zero current. B_0, the central field in the absence of magnetization, is that predicted by FEM modeling of the coils: 1.145 mT/A. Column 5 reveals the percentage by which persistent shielding currents increase the central field above that from transport current alone (column 2).

Table I: Field after each period of constant current

Current A	B_0 mT	B_+ mT	Curve fit	$\Delta B_+/B_0$ %	B_- mT	B_-/B_0 %
25	28.6	38	38.1	33.2	1.1	3.8
50	57.2	72	72.1	25.8	0.7	1.2
75	85.9	103	102.9	19.8	-1.6	-1.9
100	114.5	132	131.5	14.9	-3.9	-3.4
125	143.1	158	158.4	10.7	-7.9	-5.5
150	171.8	184	183.9	7.1	-10.5	-6.1
175	200.4	208	208.3	4.0	-19.9	-9.9
200	229.0	232	231.8	1.3	-25.0	-10.9

The analysis below postulates that the superconducting layer in ReBCO tape is so thin, and such a small fraction of the total thickness that, unless layers communicate with each other, negligible magnetization is induced by field components in the plane of the tape; only the out-of-plane field component induces magnetization. This magnetization tends to oppose changes in field intensity within the conductor, causing a lag between current and field. During a current up-ramp, the internal field will be less than from transport current alone. However, *outside* the conductor, the field perturbation from magnetization may be additive or subtractive, depending on location. A COMSOL finite-element-method program modeled the magnetization during up-ramps as relative permeability that is orthotropic, with out-of-plane component μ_y less than unity. The predictions should be quite accurate; all used a mesh four to six times finer in all directions than shown in Fig 9; Figure 11 shows the asymptotic dependence on mesh size.

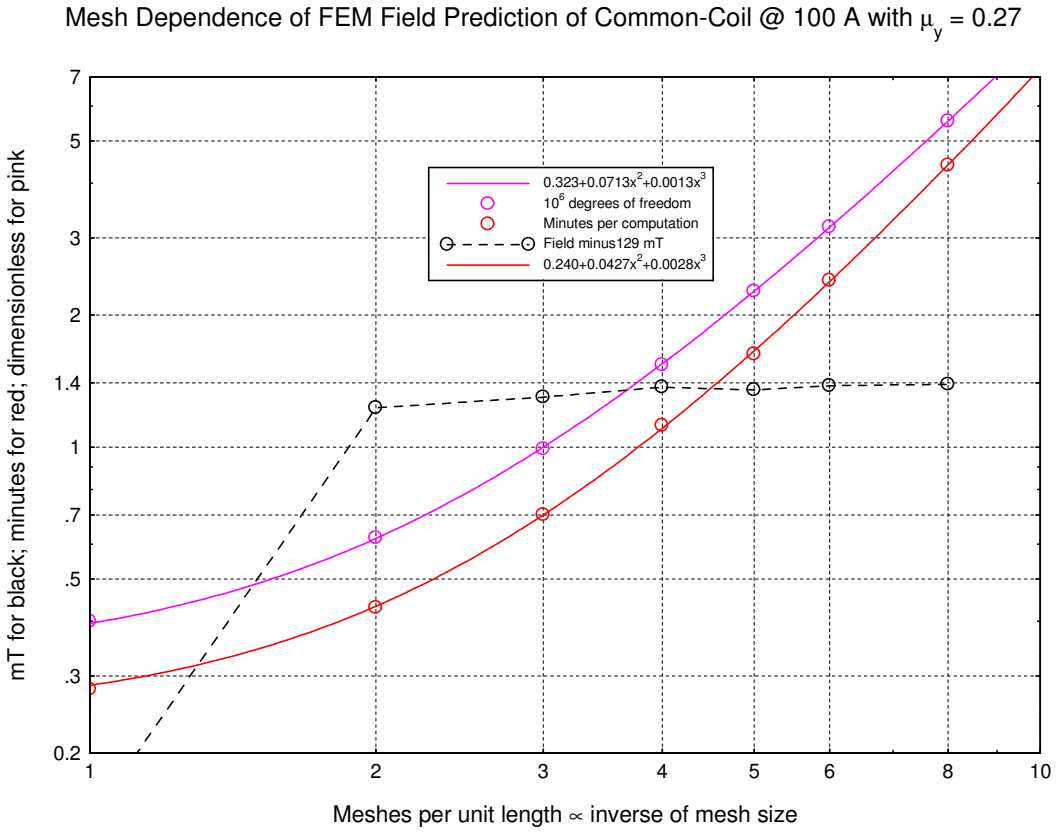

Fig. 11: Degrees of freedom, computation time, and prediction of magnetic field intensity versus mesh refinement relative to Fig. 1.

Uniform isotropic permeability of unit magnitude predicts the field from transport current alone, without magnetization. In a common-coil magnet of Fig. 9 racetracks spaced 12 mm apart, the predicted coil constant is 1.145 mT/A at the location of the Hall probe measurements—in Fig. 9, the mid-point of the lower edge of the front face, near the letter *z*. Figure 12a plots the result, at 200 A, in the $x = 0$ face of Fig. 9. The maximum field is 279 mT; the central field, 229 mT. To match the measured value of field of 232 mT, a field perturbation of 1.3%, the deduced value of horizontal, *y*, component of permeability is 0.91; the magnetization M_y ranges from −20 A/mm to +11 A/mm (see Fig. 12b).

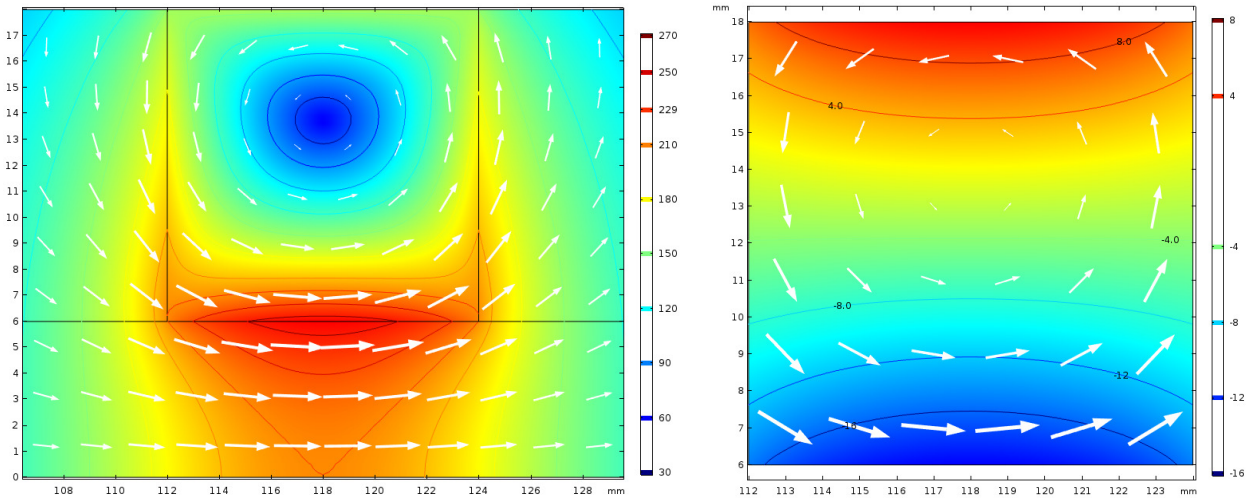

Fig. 12a&b. Field magnitude and direction (arrows) in face $x = 0$ of Fig. 9 racetrack coil in common-coil pair with gap of 12 mm. Left: Field magnitude (color & contours) at 200 A, with no magnetization; max[$B(z=0)$] = 229 mT. Right: Magnetization magnitude (color & contours) M_y predicted with relative permeability $\mu_y = 0.91$, to match measured field of 232 mT; −20 A/mm < M_y < 11 A/mm.

Figures 13 and 14 plot the predicted magnetization M_y (color & contours) and field magnitude & direction (arrows) at magnet currents from 175 A to 100 A in decrements of 25 A. The respective permeabilities μ_y to match the predicted field to the measured fields are 0.75, 0.58, 0.43 and 0.27. Note that as the transport current becomes an ever-smaller fraction of the critical current that the internal field, tilted by the ever-larger fraction from magnetization currents, becomes closer and closer to the plane of the tapes. *Caveat*: The relative size of arrows indicates relative field strength within each plot, but not from plot to plot.

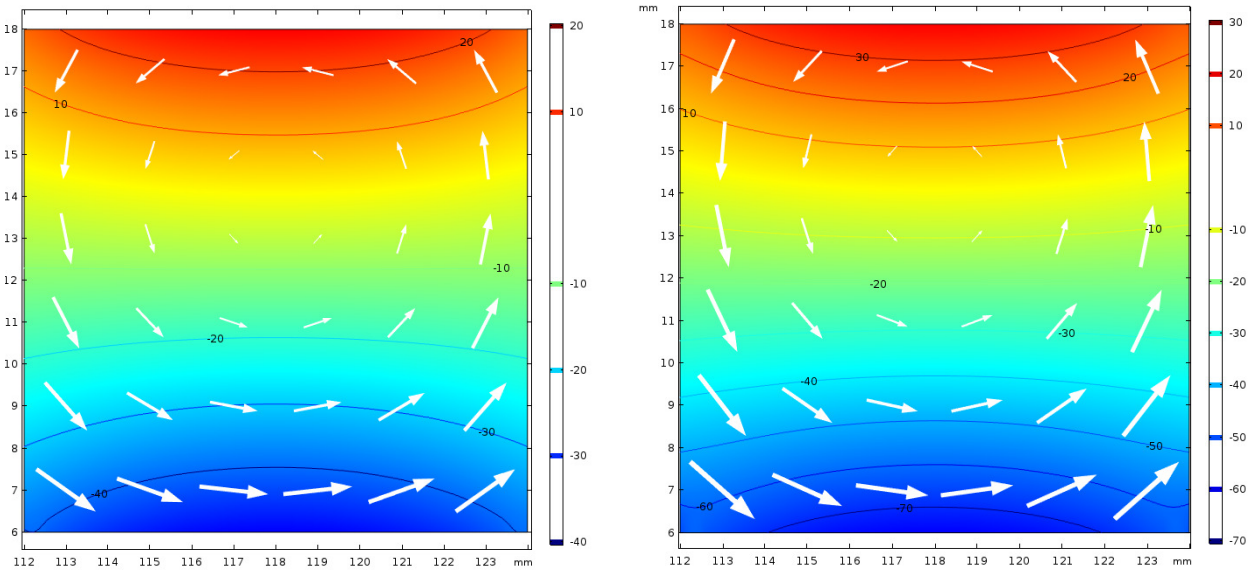

Fig. 13a&b. Magnetization magnitude M_y (color & contours) and field magnitude & direction (arrows) predicted in face x=0 of Fig. 9 racetrack magnet. Left: I = 175 A; $\mu_y = 0.75$, to match measured field of 208 mT; −51 A/mm < M_y < +27 A/mm. Right: I = 150 A; $\mu_y = 0.58$, to match measured field of 184 mT; −76 A/mm < M_y < 39 A/mm.

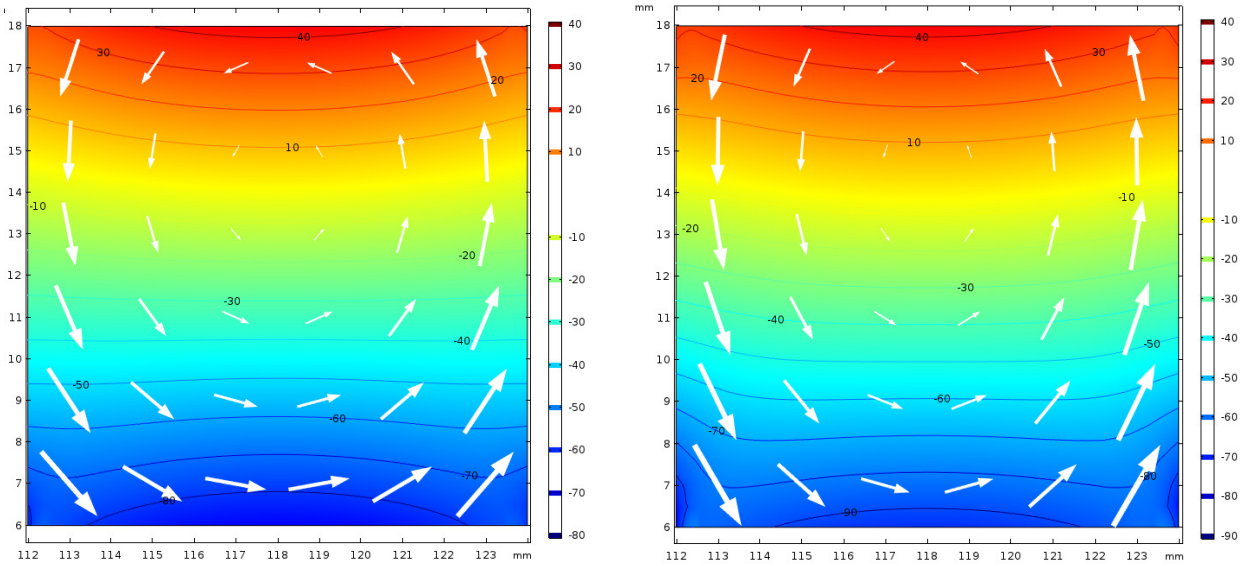

Fig. 14a&b. Magnetization M_y (color & contours) and field magnitude and direction (arrows) predicted in face x=0 of Fig. 9 racetrack magnet. Left: I = 125 A; μ_y = 0.43, to match measured field of 158 mT; −89 A/mm < M < 43 A/mm. Right: I = 100 A; μ_y = 0.27, to match measured field of 132 mT; −105 A/mm < M < 43 A/mm.

Figure 15a plots the magnetization and field for a transport current of 75 A; to match the prediction with the measured field value of 103 mT requires an out-of-plane permeability of 0.11, not far from the physically-plausible lower limit of zero. For a transport current of 50 A, no value of μ_y could make the prediction better than 1.3 mT shy of the measured field of 72 mT.

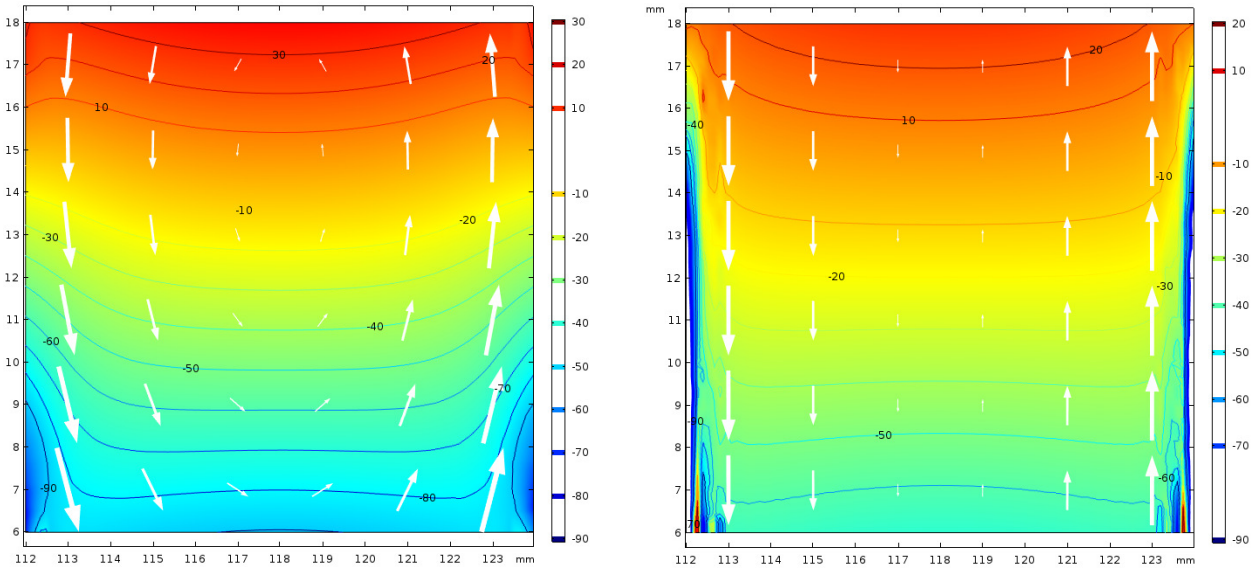

Fig. 15a&b. Magnetization M_y (color & contours) and field magnitude & direction (arrows) predicted in face x=0 of Fig. 9 racetrack magnet. Left: I = 75 A; μ_y = 0.11, to match measured field of 103 mT; −138 A/mm < M < +39 A/mm. Right: I = 50 A; μ_y = 0.001; −625 A/mm < M < 65 A/mm (color range matched to that of Fig. 15a; in white region M_y < - 200 A/mm). Predicted field = 71 mT, measured = 72 mT. Mesh is six times finer than in Fig. 9.

Figure 16 plots the dependence upon current of the out-of-plane permeability that enables the COMSOL FEM predictions to match measured values of field at transport currents from 200 A down to nearly 50 A.

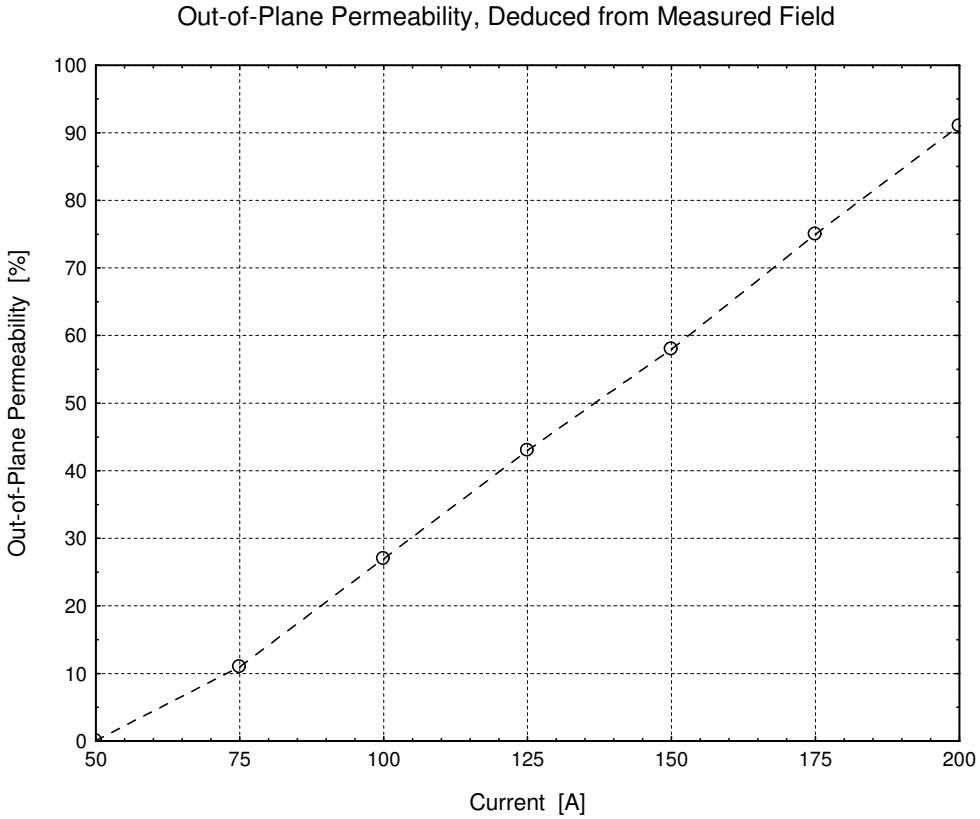

Fig. 16: Out-of-plane permeability parameter to enable COMSOL FEM prediction to match measured values of field at transport currents of 75 A to 200 A, within which range the relationship between permeability and current is linear with a slope of 0.64%/A, intersecting the horizontal axis at 58 A.

From 200 A down to 75 A the curve is precisely linear, within the accuracy of Figs. 10a &b, with a slope of 0.64%/A. Extrapolated, the line intersects the horizontal axis at 58 A, below which out-of-plane permeability would need to be less than zero to match the predicted and measured fields. To obtain agreement, the model allows magnetization in the plane of the tape, too. This may be possible, because the conductor in this magnet is two tapes in parallel, bonded by solder, allowing shielding currents to flow down one tape and back the other in magnetization current loops that are separated by the distance between the two superconducting layers, not merely the thickness of each one. The resistance of the solder crossover may be sufficiently low that the currents decay so slowly as to seem permanent.

Figure 17 plots the magnetization deduced to be necessary to match the field measured at a transport current of 25 A. The component of magnetization that is in-plane (transverse, not longitudinal) is less than, but comparable to, the out-of-plane component.

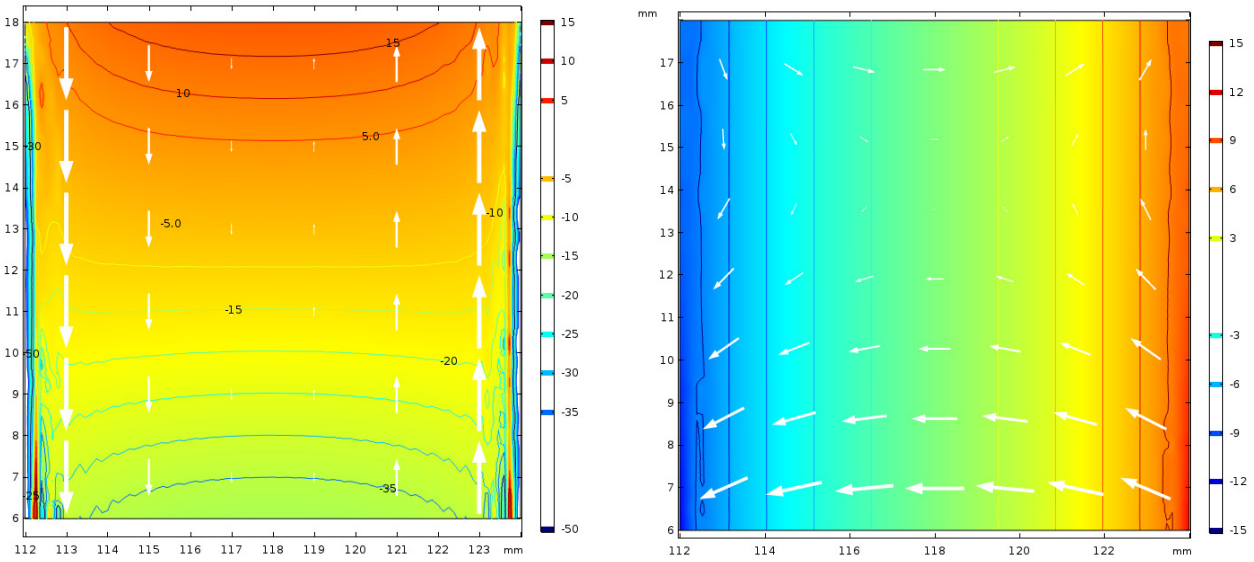

Fig. 17a&b. Magnetization (color & contours) predicted in face $x = 0$ of Fig. 9 racetrack magnet at I = 25 A; μ_y = 0.01, μ_z = 2.7, to match predicted field with measured field B_0 = 38 mT. Left: y component, −310 A/mm < M_y <40 A/mm; arrows indicate magnitude & direction of field. Right: z component, −23 A/mm < M_z < 23 A/mm; arrows indicate magnitude and direction of magnetization.

The magnetization deduced for the common-coil configuration of Fig. 9 racetracks at the end of each of the current flat tops in Fig. 10 implies a corresponding field profile in Fig. 18. Each field profile is the field perturbation introduced by the magnetization at that current. As expected with conductor so broad, the perturbations are large—e.g., 17 mT at 100 A, adding 15% to the 115 mT generated by the transport current alone.

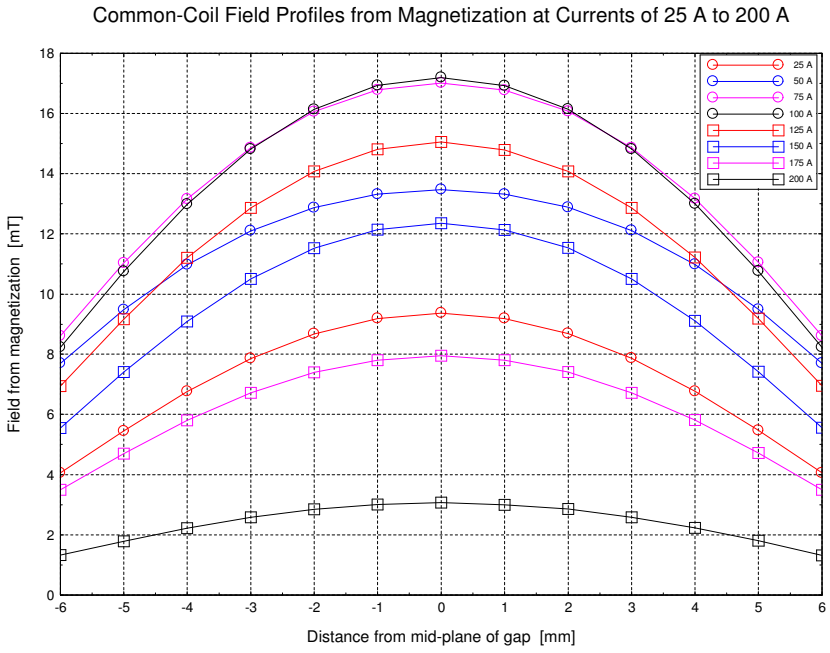

Fig. 18: Magnetic field perturbation caused by magnetization in common-coil magnets of Fig. 9 racetracks energized as in Fig. 10, with magnetization deduced by adjusting orthotropic permeability to match the measured field of Fig. 10.

Field perturbations would be less if the tape were not oriented so unfavorably relative to the ambient magnetic field. In the tape orientation considered in Figs. 12 through 15, the average out-of-plane component of field is 71% of the average field magnitude; for the butterfly geometry, it is 55%. Therefore, the more-favorable tape orientation might cut the perturbation in central field to approximately 55/71 = 78% of its previous value. In fact, the analyses below, of the butterfly geometry with orthotropic permeability retained from the analyses of Figs. 12 through 16, predict field perturbations to be approximately halved over much of the range of current—as had been observed by the measurements. Figures 19 through 21 plot the predicted field and magnetization.

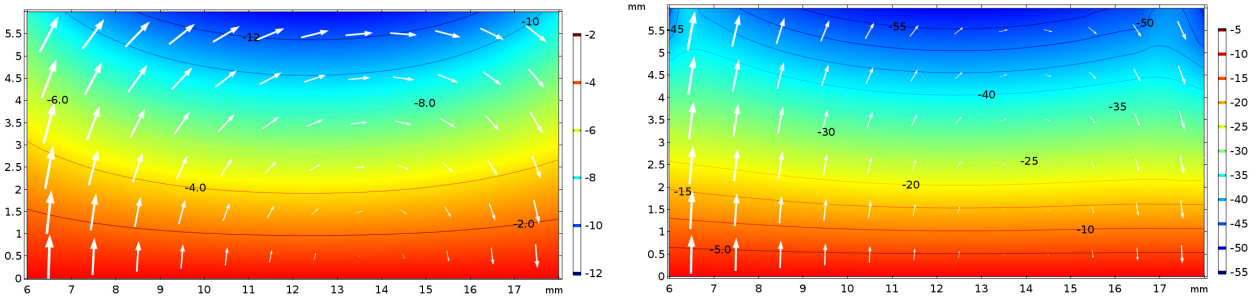

Fig. 19a&b: Field magnitude and direction (arrows) and magnetization magnitude M_y (color & contours) in face x = 0 of Fig. 9 racetrack coil in butterfly configuration with gap of 12 mm. Left: I = 200 A; μ_y = 0.91; −51 A/mm < M_y < +27 A/mm. Right: I = 100 A; μ_y = 0.27; −60 A/mm < M_y < 0.

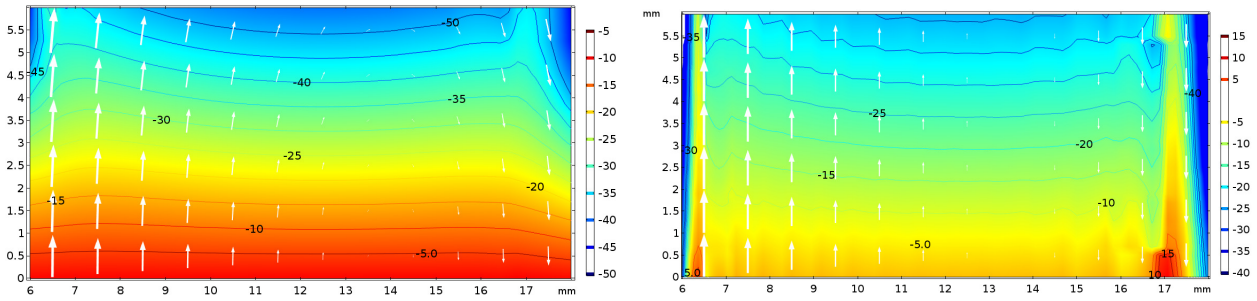

Fig. 20a&b: Field magnitude and direction (arrows) and magnetization magnitude M_y (color & contours) in face x = 0 of Fig. 9 racetrack coil in butterfly configuration with gap of 12 mm. Left: I = 75 A; μ_y = 0.11; −51 A/mm < M_y < +27 A/mm. Right: I = 50 A; μ_y = 0.001; −143 A/mm < M_y < 20 A/mm. Min data = −100; min. color = −60.

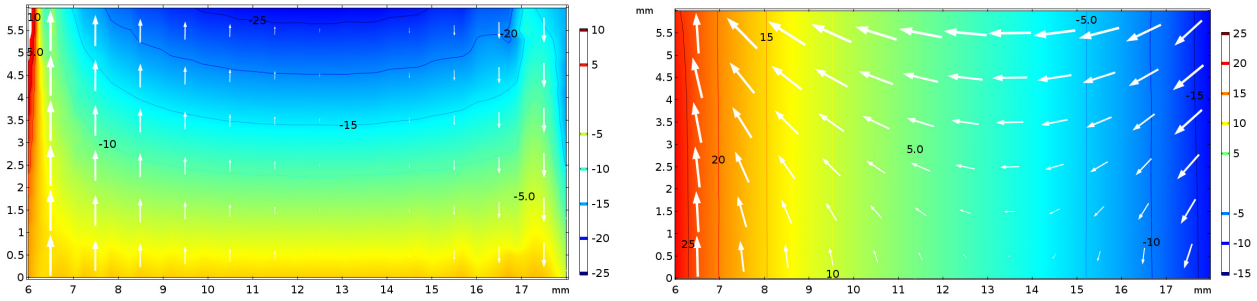

Fig. 21a&b. Magnetization predicted in face x = 0 of Fig. 9 racetrack coils in butterfly configuration at I = 25 A; μ_y = 0.01, μ_z = 2.7. Left: −310 A/mm < M_y < 40 A/mm; arrows indicate magnitude & direction of field. Right: −17 A/mm < M_z < 28 A/mm; arrows indicate magnitude and direction of magnetization.

Analogous to Fig. 18, Figure 22 plots the field generated by the magnetization predicted with out-of-plane permeability as in Fig. 16. Each field profile is the field perturbation introduced by the magnetization at that current.

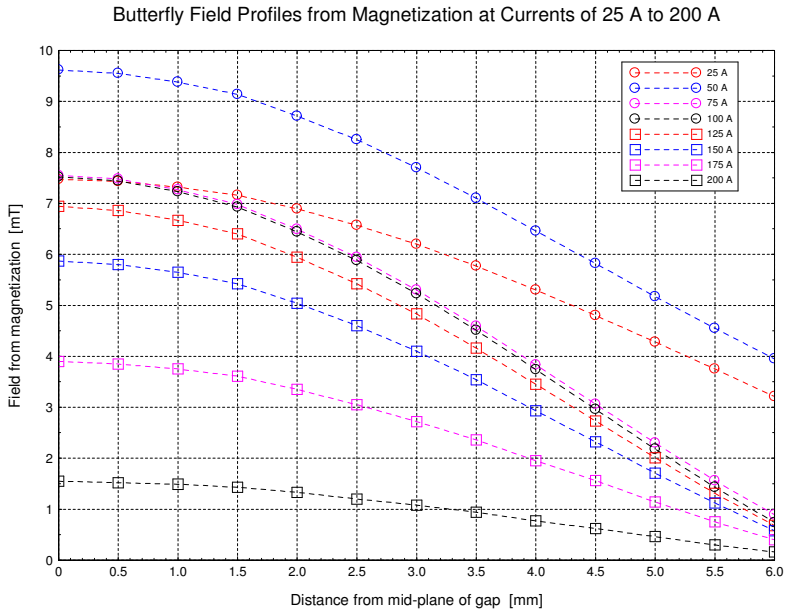

Fig. 22: Predicted profiles of field from magnetization in butterfly magnets with out-of-plane permeability of Fig. 16.

Figure 23 extracts the vertical-axis intercepts of Figs. 18 and 22 to compare the field perturbation magnitudes from magnetization in common-coil and butterfly. From 64 A to nearly 200 A, the butterfly configuration suffers less than half the field perturbation.

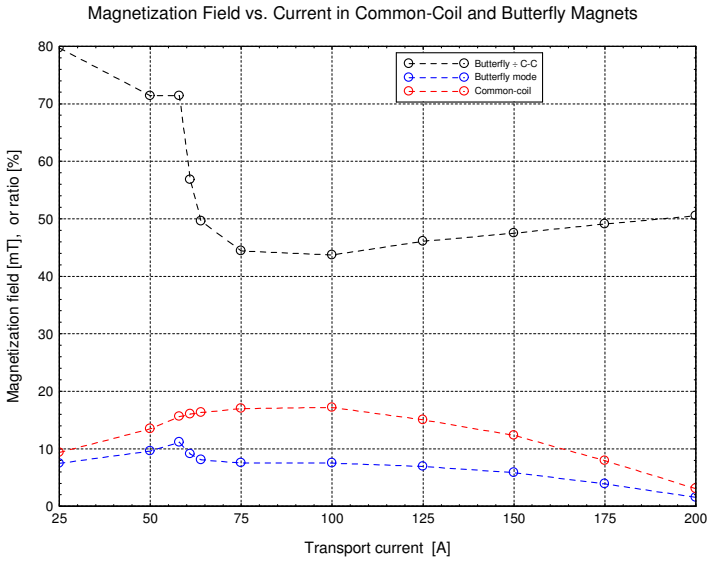

Fig. 23: Comparison of field perturbation magnitudes from magnetization in common-coil and butterfly magnets with identical out-of-plane permeability of Fig. 16. From 64 A to nearly 200 A, the butterfly configuration suffers less than half the field perturbation.

Objective 2: Proof-of-Principle Demonstration Magnet

The Proof-of-Principle (PoP) Demonstration Magnet is based on the 2-in-1 common-coil magnet design [5], in which simple racetrack coils are common to two apertures with field of opposite polarity, as required in collider magnets. Fig. 24a (left) shows the common-coil concept with a pair of racetrack coils. Fig. 24b (right) shows a magnetic model of the upper-right quadrant of BNL's Nb_3Sn common-coil dipole magnet DCC017 and, in its opening, an HTS insert racetrack dipole in the hybrid magnet built and tested under this STTR. The two sets of Nb_3Sn coils are in red; the HTS coil displays in red to blue the computed range of field—8.7 T at its inboard edge, 7.6 T at its outboard edge—with 635 A in the HTS coils and 8 kA in the Nb_3Sn coils. The iron yoke is in blue.

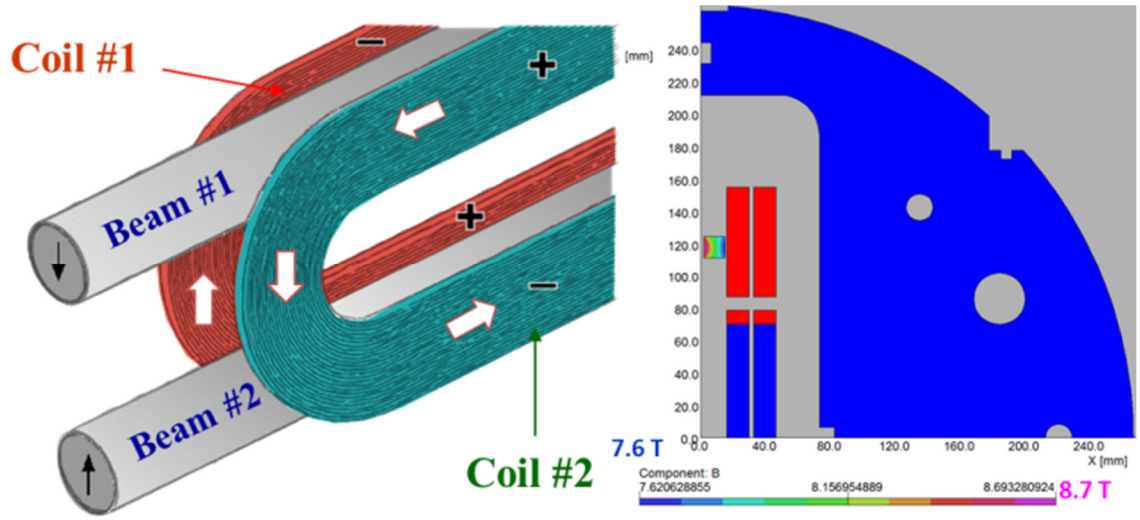

Fig. 24a&b. Concept of common-coil design (left), with a pair of racetrack coils producing field in opposite directions in two apertures. Right: Upper-right quadrant of hybrid magnet tested under this STTR, with an HTS racetrack dipole (immediately to the right of label "120.0") in the opening of BNL's common-coil magnet DCC017.

As a part of this Small Business Technology Transfer (STTR) program, a hybrid Proof-of-Principle dipole was assembled and tested in a strong background field. Enabling this ambitious accomplishment was a facility unique to BNL: a Nb_3Sn common-coil dipole [4] that has a large opening in which HTS racetrack coils can be inserted without the prohibitive expense in time and money to disassemble and reassemble the magnet (see Fig. 25 and Table I). The new HTS coils made direct contact with the Nb_3Sn coils and became an integral part of the HTS/LTS hybrid magnet structure. The magnet was tested in various configurations and combinations of current in the Nb_3Sn and HTS coils, up to 10 kA in the Nb_3Sn magnet and 800 A in the HTS one.

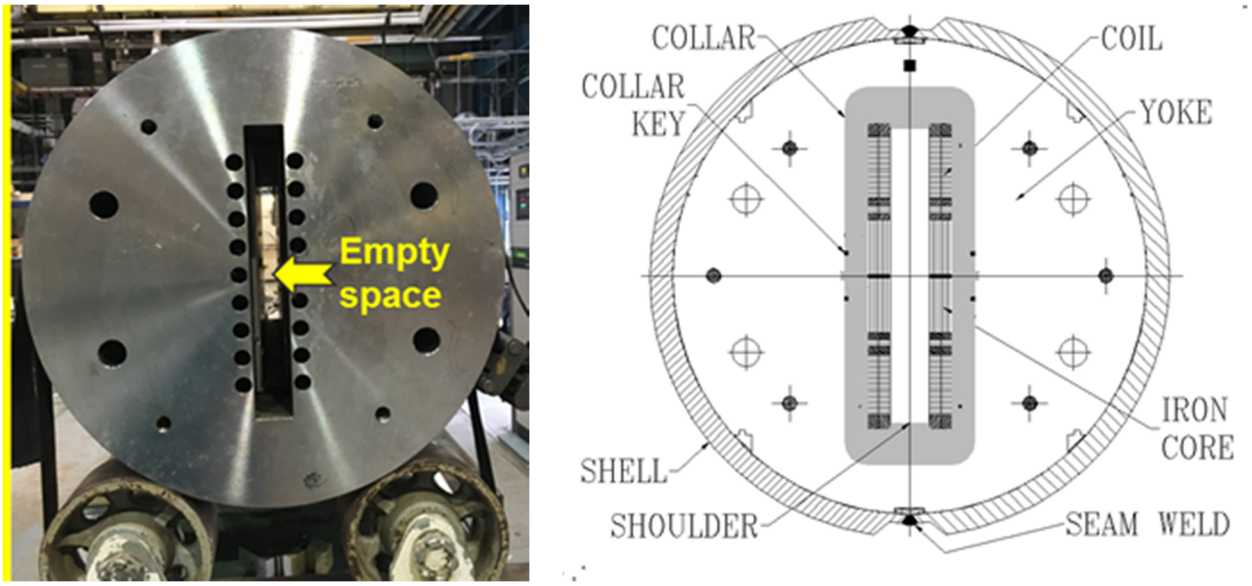

Fig. 25. Left: BNL's Nb_3Sn common-coil dipole magnet, with its large opening for testing coils. Right: Sketch showing this opening (31 mm wide by 338 mm high) between the Nb_3Sn coils.

TABLE I

PARAMETERS OF THE LTS DIPOLE DCC017 FOR HTS INSERT COILS

Dipole design	2-in-1 common-coil
Coil technology	Nb_3Sn, react & wind
Horizontal aperture (clear space)	31 mm
Vertical aperture (clear space)	338 mm
Number of LTS coil layers	Two
Computed quench current	10.8 kA
Peak field at quench current	10.7 T
Computed quench field @4.2 K	10.2 T
Coil length (overall)	620 mm
Coil straight section length	305 mm
Coil inside radius in ends	70 mm
Yoke length	653 mm

Figure 26 shows field contours and streamlines in greater detail—26a for all coils, and 26b for the HTS coils alone.

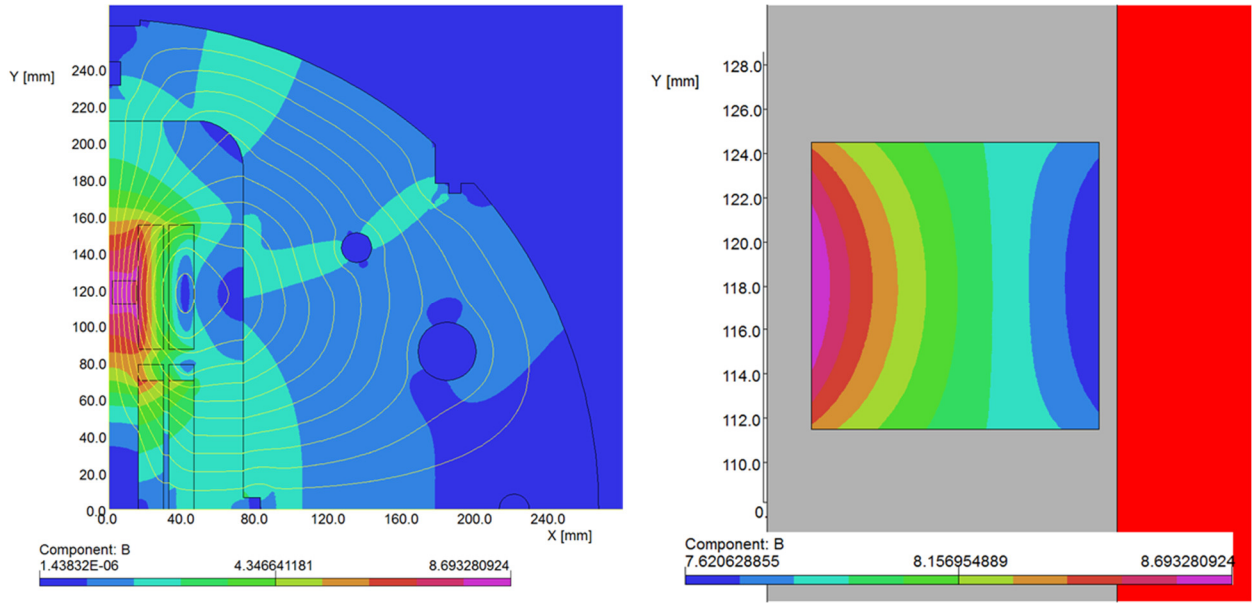

Fig. 26a&b. Left: Magnetic model of upper-right quadrant of magnet as tested, showing field contours and streamlines with Nb_3Sn coils at 8 kA and HTS coils at 635 A. Right: Detail of field contours on HTS coil.

Testing was limited by the current leads on the test stand. Fig. 27 shows the 3D model of the case had the testing current not been limited by the leads.

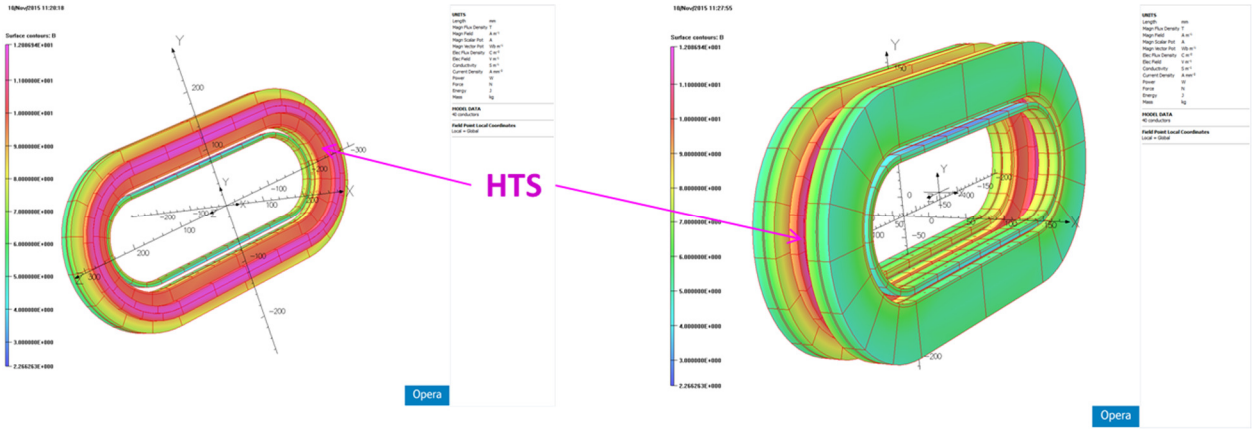

Fig. 27a&b. 3D magnetic model showing Nb_3Sn and HTS coils with field intensity indicated by color. For clarity, 27a shows only the inboard side; 27b shows both sides.

MAGNET CONSTRUCTION

Two pancake coils were wound with 12 mm wide, 4-ply HTS tape (two plies of ReBCO and two of copper) from American Superconductor Corporation (ASC). The cross-section of the coil was chosen to be square to facilitate comparison during magnetization studies (see next section). Each coil had 35 turns of 25 m of double HTS tape, a total of 100 m for the entire magnet. Figure 28 shows winding of the racetrack coil with the BNL universal coil winder; turn-to-turn insulation was Nomex tape 50 microns thick and ~12 mm wide.

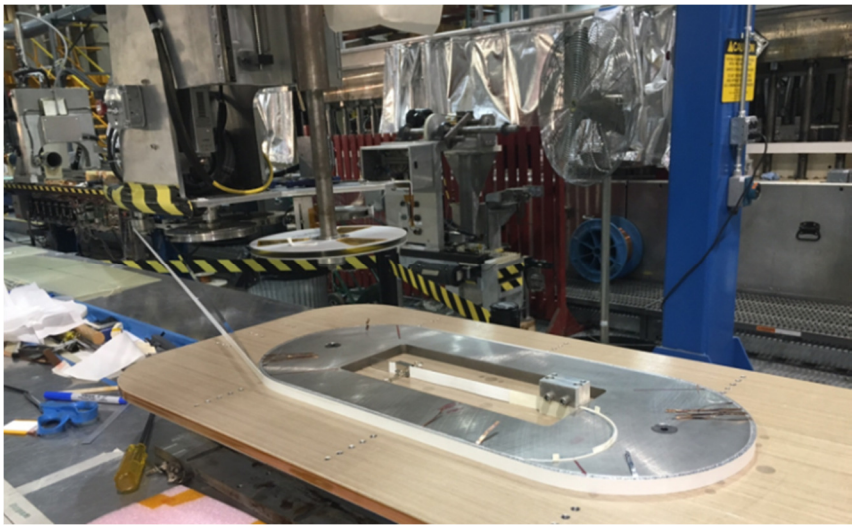

Fig. 28. Coil being wound by universal coil winder with 4-ply ASC tape and Nomex insulation

After a number of 77 K tests in liquid nitrogen, the HTS coils were installed inside the LTS magnet. Figure 29a is a schematic of the hybrid design, with the new HTS coil structure; the complete hybrid magnet assembly is shown in Fig. 29b (right).

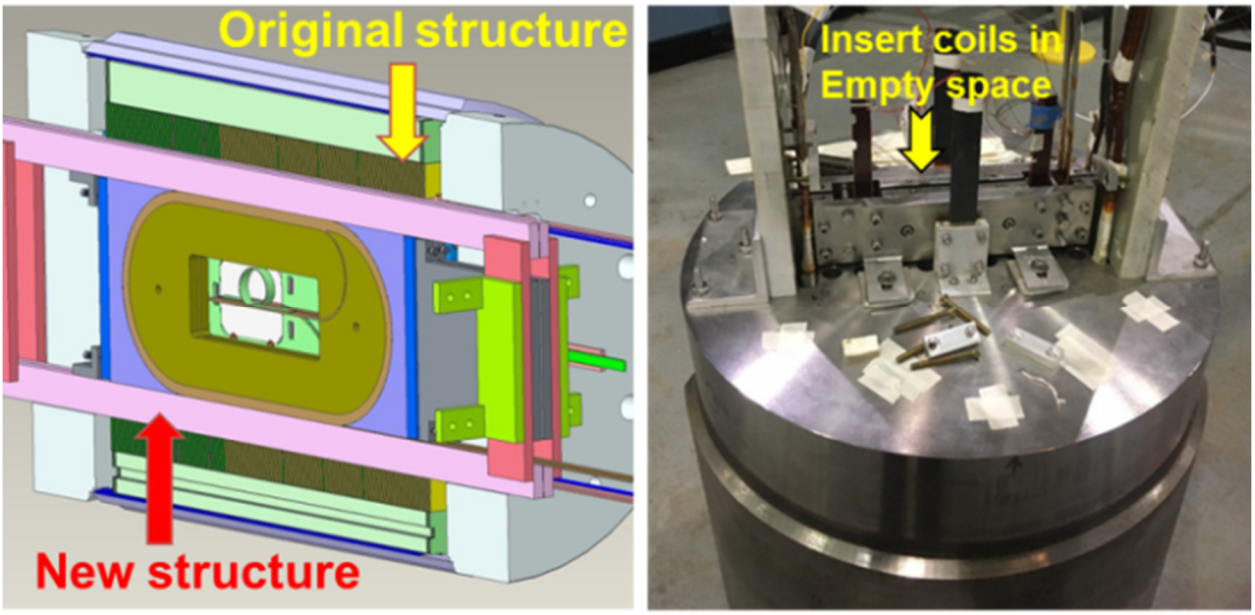

Fig. 29a&b. Left: Schematic design of the hybrid magnet. Right: DCC017 with the new HTS coils inserted.

Figure 30 shows intermediate steps with two HTS coils connected in series in the common-coil configuration, and a practice run of inserting HTS coils inside the Nb_3Sn dipole DCC017 magnet. The two HTS coils were internally connected in the middle of the magnet, where the field is low, with an innovative flexible splice that allowed the HTS coils to separate slightly when loaded by the Lorentz forces, without significantly straining the splice.

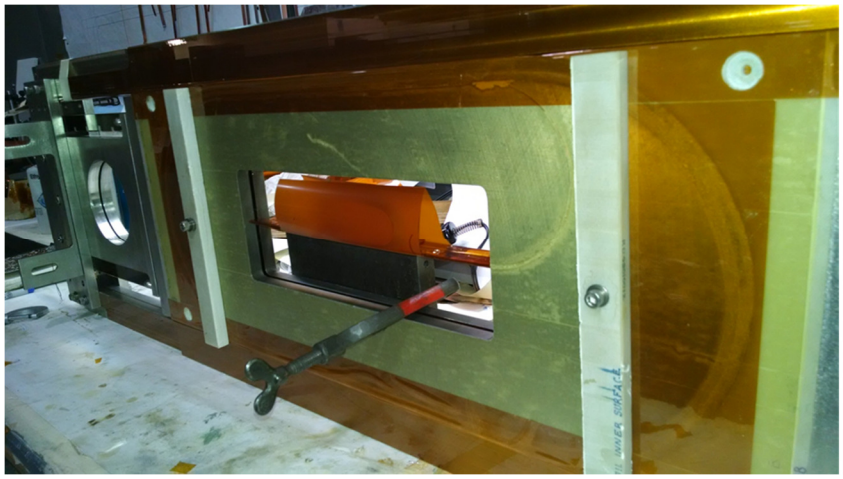

Fig. 30a&b. Left: HTS coils in common-coil configuration. Right: Hybrid magnet of DCC017 and new HTS coils.

HYBRID MAGNET TEST

Tests were performed at 4 K with combinations of powered coils—HTS alone, Nb_3Sn alone, and both together. The Nb_3Sn magnet DCC017 performed well despite a decade in storage, reaching 10 kA (92% of the short sample) without a quench (Fig. 31a). The maximum hybrid dipole field was ~8.7 T (a record at the time), with ~7.6 T coming from the Nb_3Sn coils at 8 kA, limited by the external leads, not the coils. The HTS coils were powered at various background fields (a) in cycles of 0 A to 500 A and back, without quenching, and then (b) to quench (see Fig. 31b). No degradation in the performance of HTS coils was observed from the multiple quenches—this despite being allowed to quench like an LTS coil, with a difference-voltage threshold as high as 200 mV (see Fig. 32).

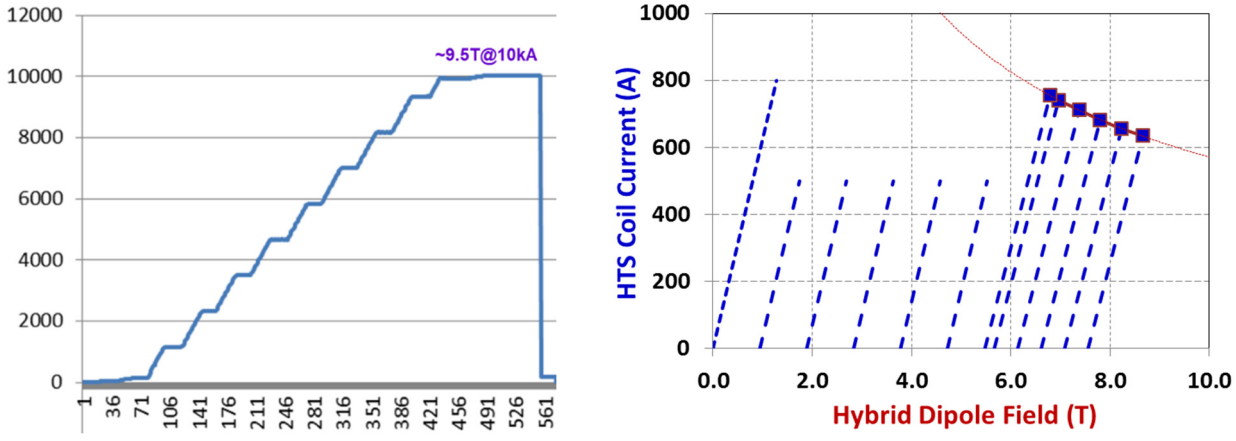

Fig. 31a&b. Left: Ramping up of current in Nb_3Sn coils of DCC017. Despite a decade in storage, the magnet reached 10 kA (~92% of the short sample) without a quench. Right: Performance of hybrid dipole magnet vs. HTS current for various fields from the Nb_3Sn magnet.

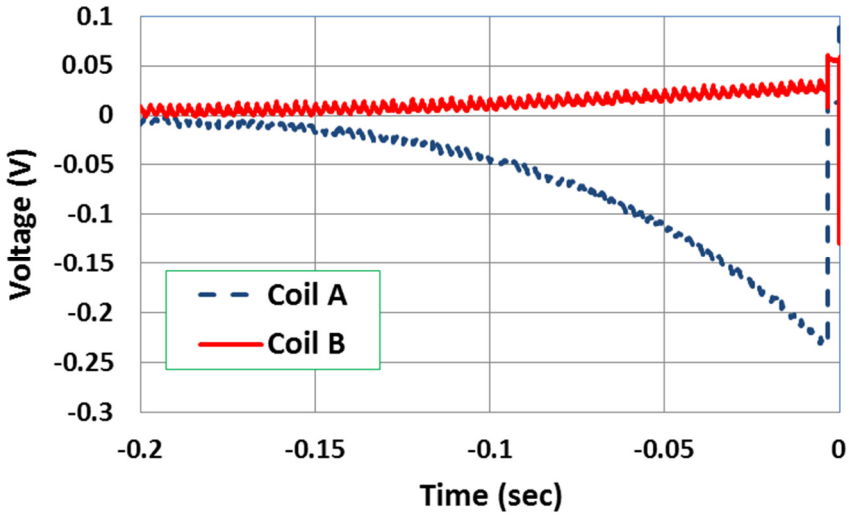

Fig. 32. Quench detection in HTS coils, with a difference-voltage threshold of 200 mV. The BNL advanced-detection and rapid-energy-extraction system protected the HTS coils during multiple quenches.

The BNL advanced-quench-protection system [10, 32] and rapid-energy-extraction strategy worked well. The basic hardware is shown in Fig 33.

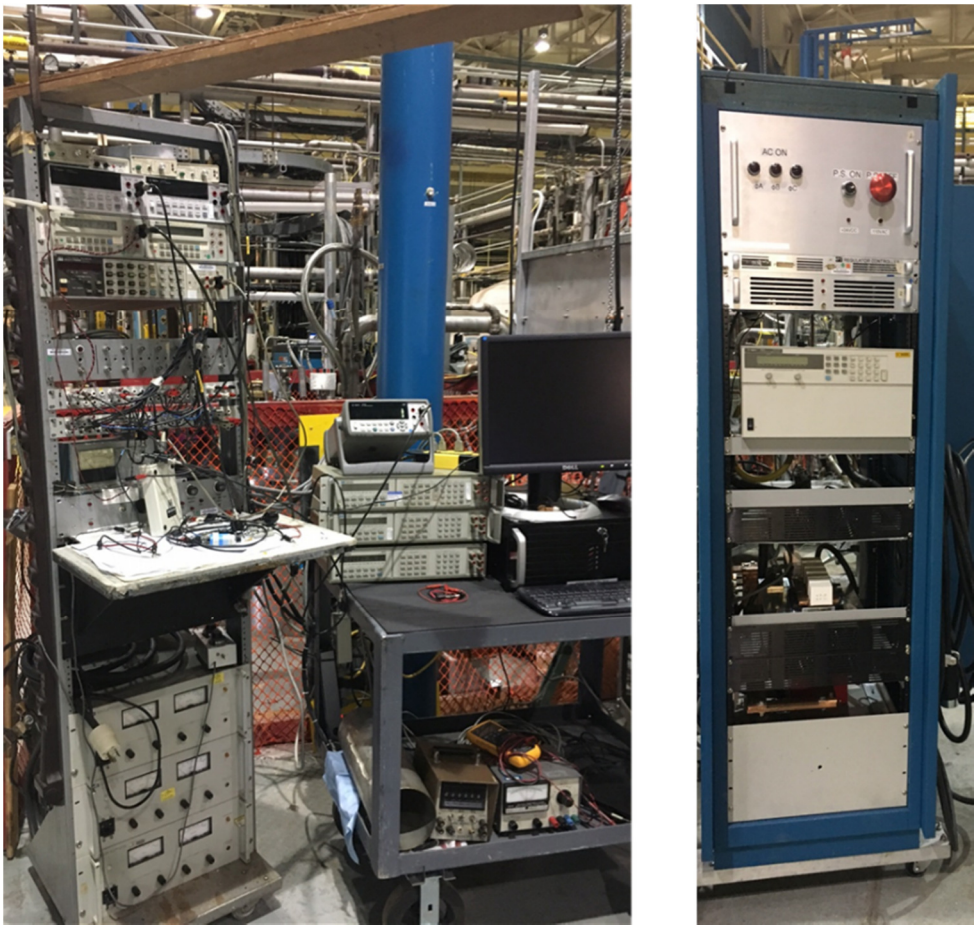

Fig. 33. Hardware of the PBL/BNL advanced-detection and rapid-energy-extraction system.

Figures 34 and 35 diagram the HTS/LTS quench detection/protection system and the energy extraction system.

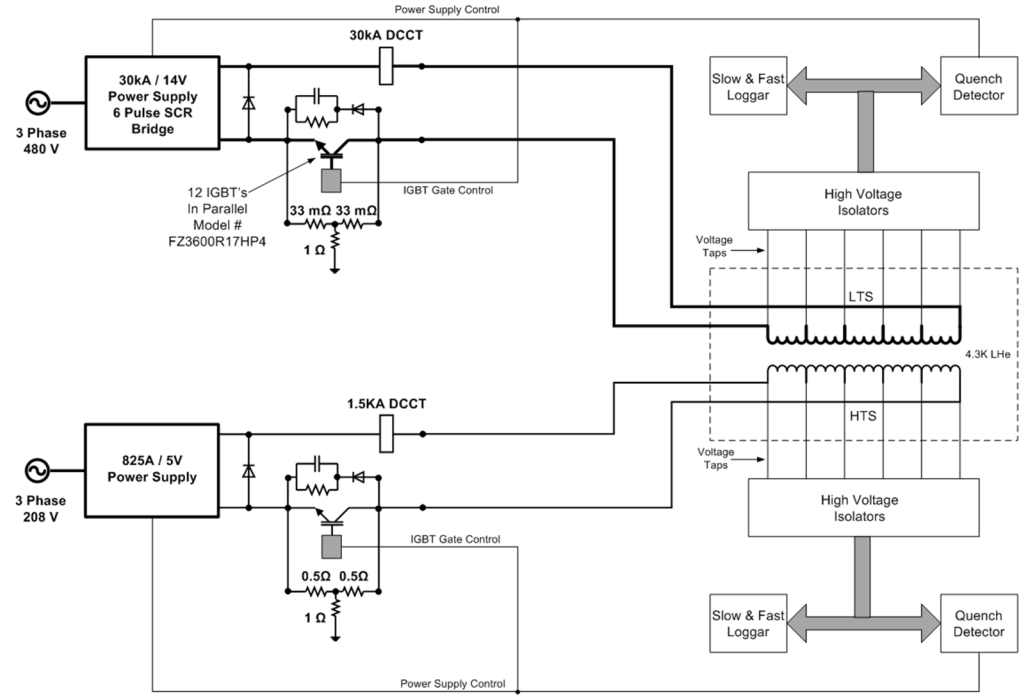

Fig. 34. Diagram of the HTS/LTS hybrid quench-detection/protection system.

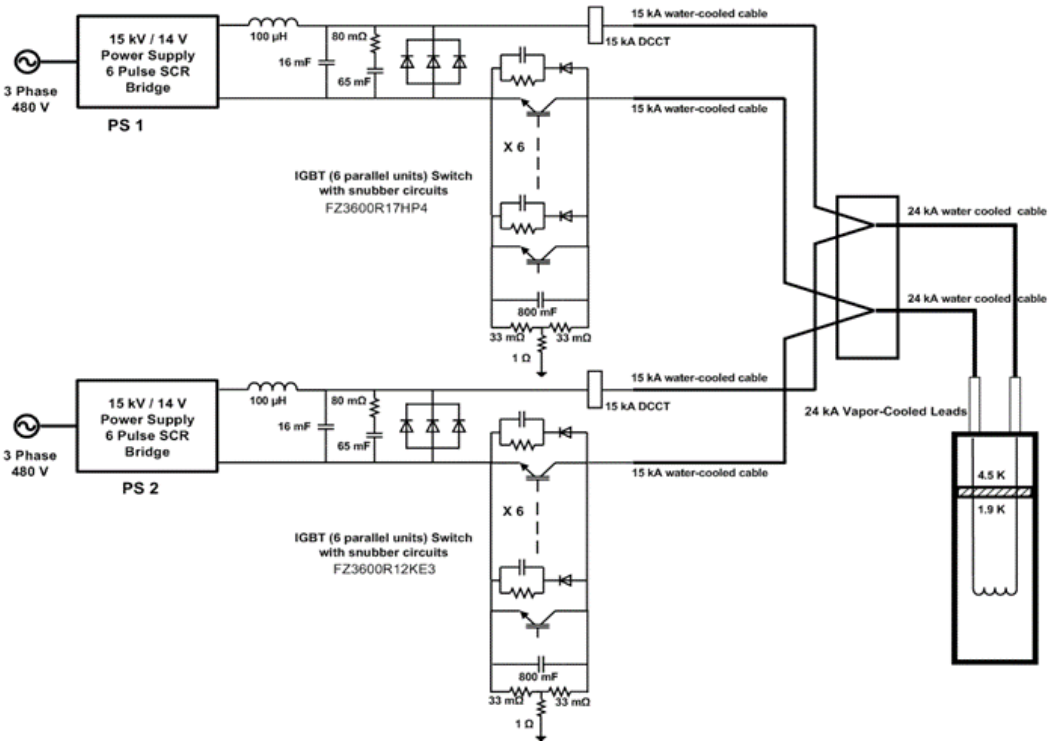

Fig. 35. Diagram of the energy extraction system for HTS/LTS hybrid magnet.

The HTS and LTS coils are coupled magnetically, as can be seen from Fig. 36, quenching of the HTS coil feeding energy to the LTS magnet, slightly increasing its current.

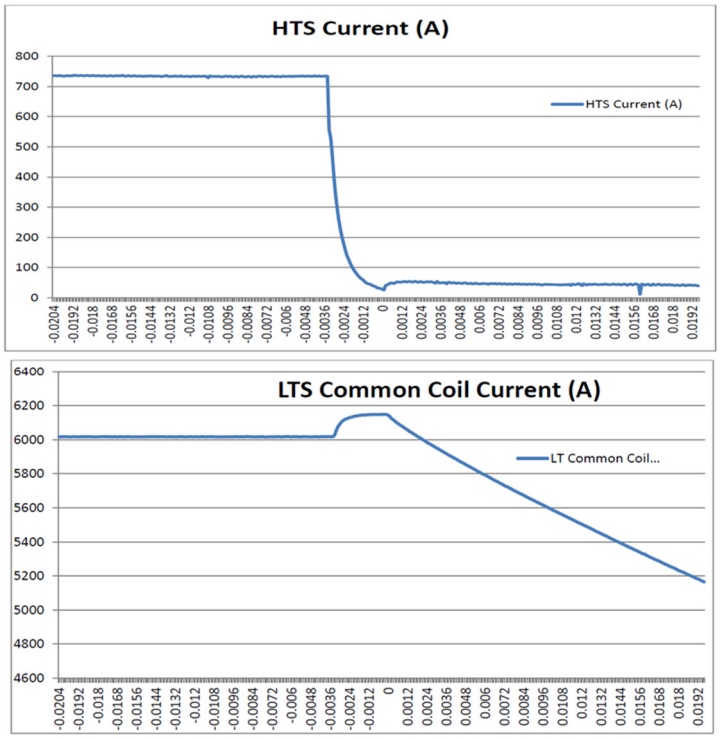

Fig. 36. Evidence of coupling between HTS and LTS coils.

The current in the two magnets decayed with much different time constants (see Fig. 37) because of the greatly differing inductances of their power supplies. A very encouraging finding of the test was that the HTS coils suffered no degradation despite being allowed to quench like LTS coils, with a relatively high difference-voltage threshold.

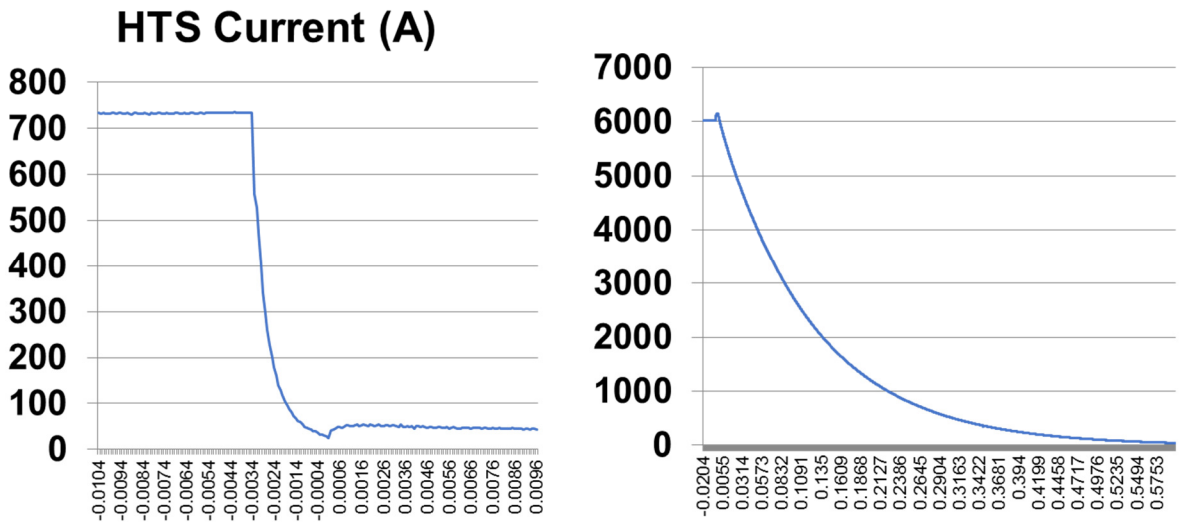

Fig. 37. Differing time constants of the energy extractions of HTS and LTS coils in the PBL/BNL hybrid magnet.

MAGNETIZATION MEASUREMENTS

Before the ReBCO coils were installed inside the Nb_3Sn magnet, they were tested in liquid nitrogen. Magnetic field measurements were made along the axis of the aperture using a Siemens SBV604 Hall probe. The common-coil set-up is shown in Fig. 38, with the horizontal spacing between two coils (a) 12 mm and (b) 3 mm, the maximum beyond which the coil pair would not fit in the opening of magnet DCC017 for testing. In this configuration the field on the median plane is predominantly perpendicular to the wide face of the conductor, and the magnetization is expected to be large.

The effect of the induced magnetization shows up most dramatically at zero transport current after an excursion to high current. Figure 39 shows the result of raising the current in 25 A steps to 200 A with a return to zero between each step, with a magnet gap of 12 mm. An interval (5-8 minutes) was allowed both at peak current and at zero for the field to stabilize. For the geometry of Fig. 38, the residual or trapped field depends quite strongly on the maximum current reached and is opposite in sign to the powered field (see Fig. 40). The slow field changes that occur at this end of each step are pronounced in this coil configuration.

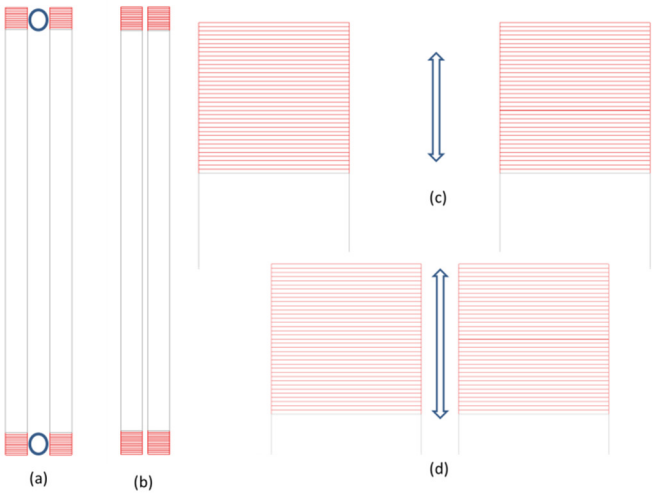

Fig. 38. Schematic of relative coil sizes and Hall probe location during tests in common-coil configuration. Coil separation is 12 mm in (a) and (c), and 3 mm in (b) and (d); (c) and (d) clarify the tape orientation.

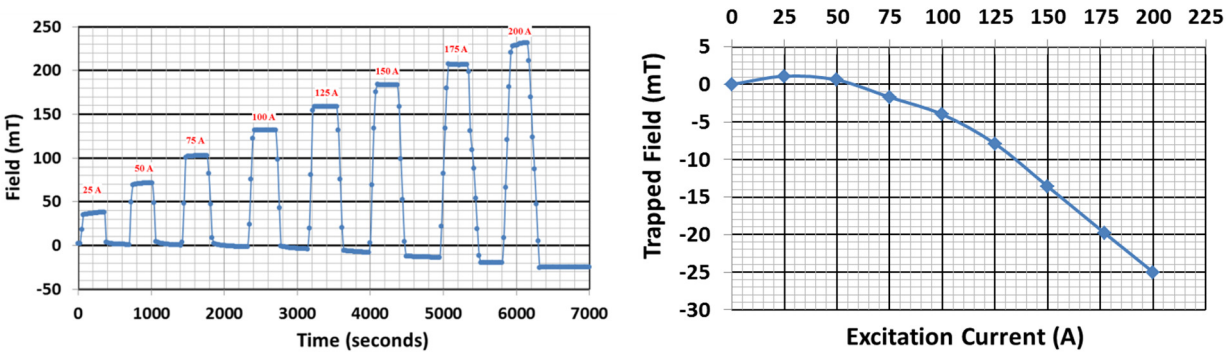

Fig. 39a&b. Left: Residual fields at zero current after current ramps incremented by 25 A to 200 A. Right: Field trapped by HTS coil after each zero-current holding period in Fig. 39a.

For the coil arrangement of Fig. 40, in which the conductor is parallel to the field at the median plane of the inter-coil gap, the trapped field has the same polarity as the normal field and resembles the residual field of a solenoid of the same cross section. Figure 41 plots the field along the coil axis for the magnetization field compared to a powered curve. The maximum trapped field in this configuration typically is less than half of the field in the perpendicular conductor orientation.

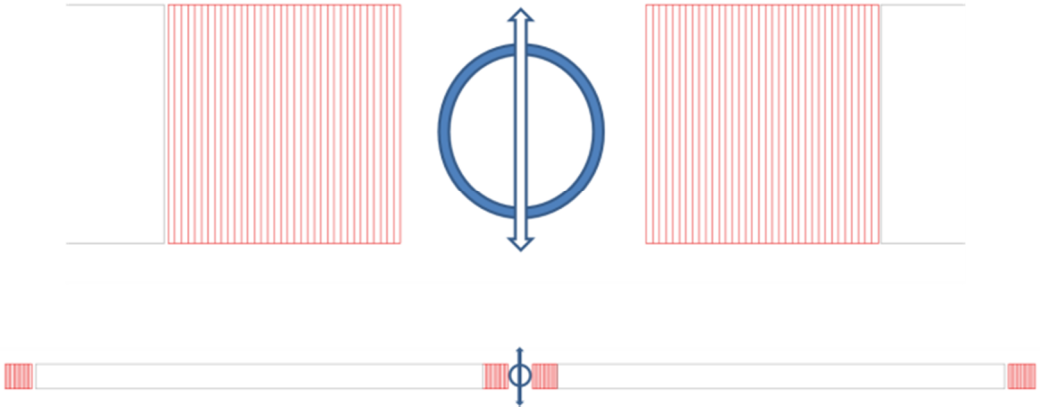

Fig. 40a&b. Schematic of Hall probe location and tape orientation (upper drawing) and relative coil sizes (lower drawing) during tests in side-by-side configuration.

While assembled in the stainless steel frame but before insertion in the high field magnet, the coils were re-measured at 77 K. Figure 41a plots the field vs. current for two successive excursions to 200 A. On the first cycle the conductor begins with no magnetization just after cool-down and ends with magnetization that generates a substantial negative field at the Hall probe. The second cycle follows the down half of the first cycle but slightly displaced toward higher fields. The second down cycle is identical to the first one; subsequent current cycles duplicate the second one. It takes approximately 20 A to restore zero field.

The effect of the magnetization currents is more apparent if plotted as the transfer function, B/I, as shown in Fig. 41b. With the coil separation reduced to 3 mm the negative trapped field is 2½ times as large as for the 12 mm spacing, whereas the increase in field from just the transport current was about 50%.

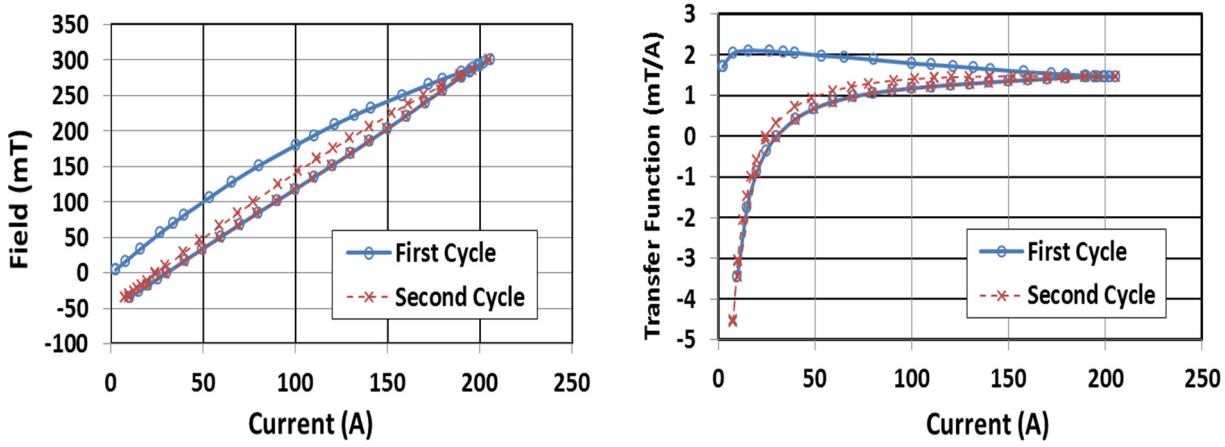

Fig. 41a&b: Left: Field vs. current during first two cycles. Right: Transfer function during first two cycles

When tested at 4.5 K, the magnetization currents induced in the HTS conductor by the much higher field of the Nb_3Sn magnet trapped field as high as ~500 mT when energizing the HTS and Nb_3Sn coils to test and set parameters for the quench protection system. At each applied field the insert coils were energized to 500 A (Figs. 31b & 42). Figure 42 shows the field from the HTS coil (offset introduced to start curve from zero) vs. current in the HTS coils for a background field of ~2 T (2 kA in the Nb_3Sn coils). The field at the center of the aperture starts lower than the applied field and rises with the HTS current but returns to an even lower field when the HTS current returns to zero.

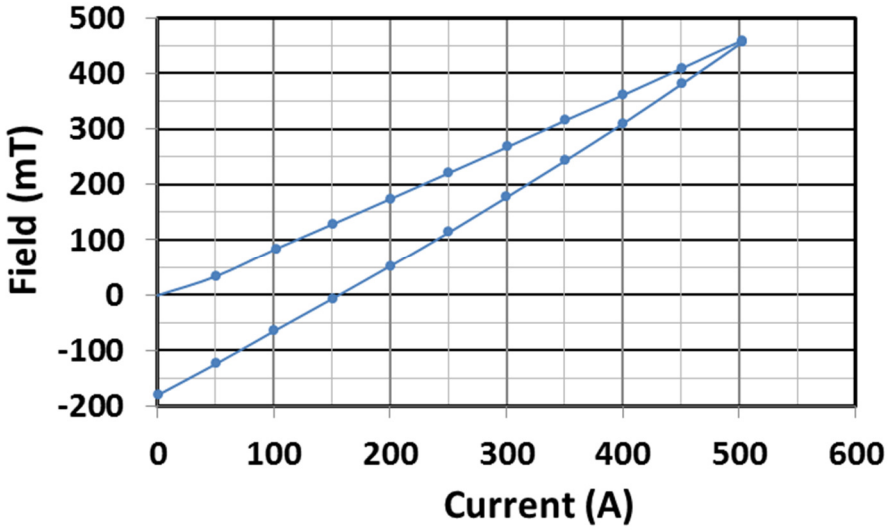

Fig. 42: Field from HTS coil vs. current in background field of ~2 T (offset introduced to start curve from zero).

The large negative residual field persisted for hours with both coils de-energized, slowly decreasing in magnitude as shown in Fig. 43.

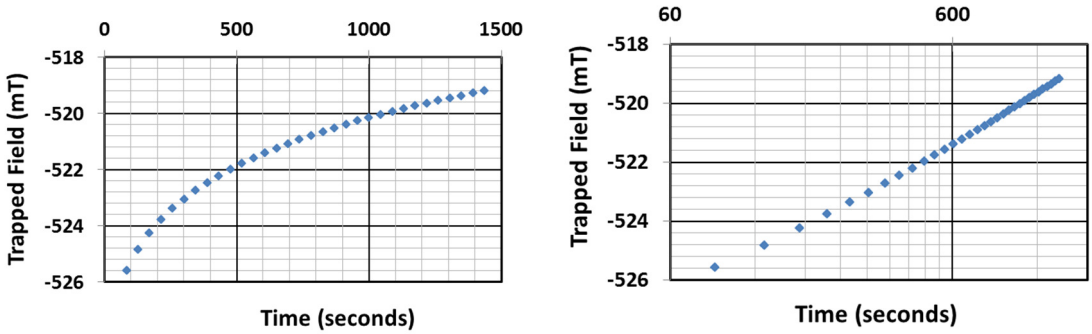

Fig. 43a&b. Decay of trapped field with time. (a) linear time scale; (b) logarithmic scale.

Figure 43b reveals that the trapped field decreases about one percent per decade. The first percent takes about one hour, and the next percent 10 hours. All 4 K measurements were performed with the HTS coils in the LTS coils, and therefore with a gap of 3 mm.

Objective 3: Optimization of the High Field Accelerator Magnet Design

An HTS coil pair of ReBCO tape was tested in the background field of BNL's Nb_3Sn common-coil dipole DCC017. Its HTS tapes were oriented unfavorably (large out-of-plane component to the field), limiting the current capacity of the conductor but simplifying the leads. As shown in Fig. 44, the Nb_3Sn magnet DCC017 also can accommodate the tape orientation that increases current capacity and reduces magnetization.

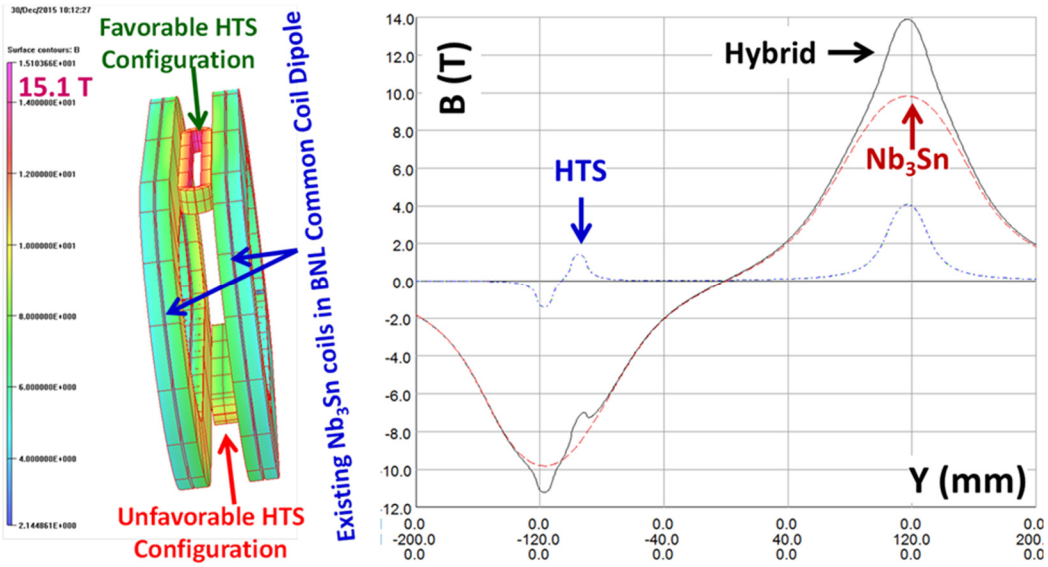

Fig. 44. Left: Alternative orientations of HTS racetrack coils inside BNL's Nb_3Sn common coil dipole in favorable and unfavorable tape orientations. Right: Field profiles at 600 A/mm^2 for the favorable orientation and 200 A/mm^2 for the unfavorable one.

Field, Homogeneity, Stress, Strain & Deformation of Dipole with Tilted HTS Tape

Among the analytical efforts of this STTR was to study the field, field homogeneity, stress, strain and deformation in an illustrative design for a hybrid HTS/LTS dipole for 20 T. The design shown below has robust horizontal and vertical webs to support the huge magnetic loads that are associated with such a magnet. Its field homogeneity can be excellent, at least in theory—i.e., if undegraded by magnetization and/or imperfect placement of the conductor. Figure 45a shows its coil-block geometry and field magnitude (color & contours) and the direction (arrows) of the ambient field seen by the high-temperature superconductor. Within each conductor block the HTS tape is tilted to match the average direction of the ambient magnetic field.

Iron contributes 7% to the field of the magnet and reduces its fringe field by an order of magnitude. The 5-gauss reach of the magnet has a radius of ~4.6 m, compared to over ~13 m without iron. In the absence of conductor magnetization, the design is capable of accelerator-quality field homogeneity of one part in 10^4 over a diameter of nearly 3 cm (see Fig. 45b). Achievement of this homogeneity required zeroing four inhomogeneity coefficients—quadrupole, sextupole, octupole and decapole. The polynomial that describes the field inhomogeneity is 10^{th} order; its first non-zero term beyond the dipole term is $c_{10}\, r^{10} \cos(10\,\theta)$.

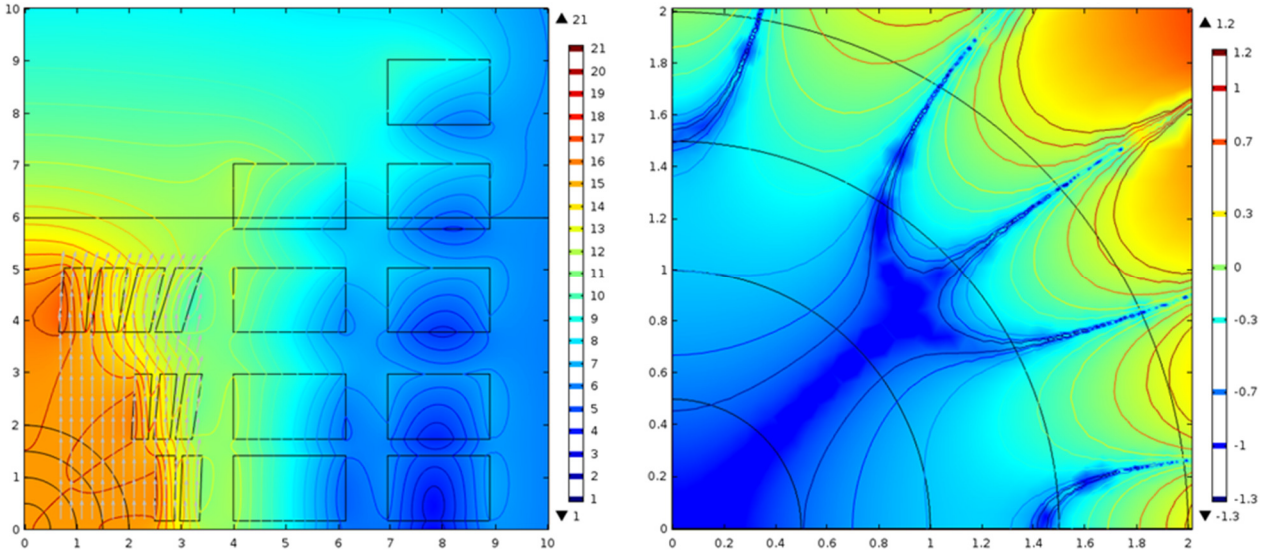

Fig. 45a&b. 20-T hybrid dipole with tilted HTS tape. Left: Coil-block geometry and field direction (arrows) and magnitude (color & contours). B_{max} is 22 T in the HTS, 14 T in the Nb_3Sn, and 7 T in the NbTi (the lower-right three conductor blocks, with $x > 7$ cm, $y < 5$ cm). Right: Field inhomogeneity, $\Delta B_y/B_0$, in parts in 10^4; successive contours are [$10^{-1.3} = 0.05$ (navy), 0.1, 0.2, 0.5, 1, 2, 5, 10, $10^{1.2} = 16$ (maroon)].

The iron is used very efficiently: never fully saturated, but typically within ~5% of being so. Despite being so highly magnetized, almost all of the iron has a permeabilty that is at least 10 (Fig. 46a). Maintaining a high permeability almost everywhere, avoiding excessive iron saturation anywhere, helps to maintain field homogeneity over the complete range of fields, which is facilitated if the field contribution from the iron, like that of the coils, is proportional to the magnet current.

The consequent degradation in field homogeneity can be severe at currents far from the design value. For example, the peak-to-peak field homogeneity (max B_y – min B_y)/B_0 over a diameter of

2 cm degrades two-hundredfold from 0.1×10^{-4} at the design value of 20 T to 20×10^{-4} at fields below 3 T. The design of Figs. 45-46a, on the other hand, maintains essentially all of its 20-T field homogeneity at all lesser fields (see Fig. 46b). Its 20-T field homogeneity is inferior only because of fewer iterations to reduce error coefficients c_4 through c_8.

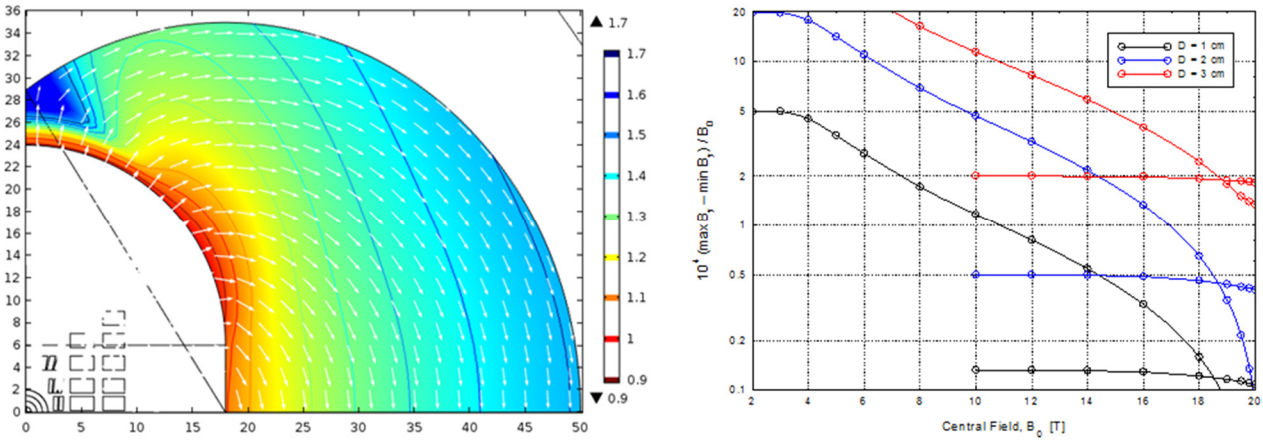

Fig. 46a&b. Effects of iron saturation. Left: Permeability (color & contours) and magnetization direction (arrows) of 20-T dipole of Fig. 45; almost all of the iron has a permeabilty of at least 10. Right: Field dependence of peak-to-peak field inhomogeneity (max B_y – min B_y)/B_0, in parts in 10^4 within diameters of 1 cm, 2 cm and 3 cm for two magnets. Flat curves: magnet of Figs. 45-46a; sloped curves: magnet degraded by saturation when $B_0 > 3$ T.

Figure 47a&b estimates the volumetric strain and total deformation within the magnet. The finite-element model recognizes that the conductor not only is much less stiff than the support structure, but also is orthotropic, being less stiff horizontally than vertically. The model does not yet acknowledge slippage between conductor blocks and supporting structure, but does introduce slender air gaps at any boundary across which the stress is expected to be tensile, thereby opening a gap between the conductor block and the support structure.

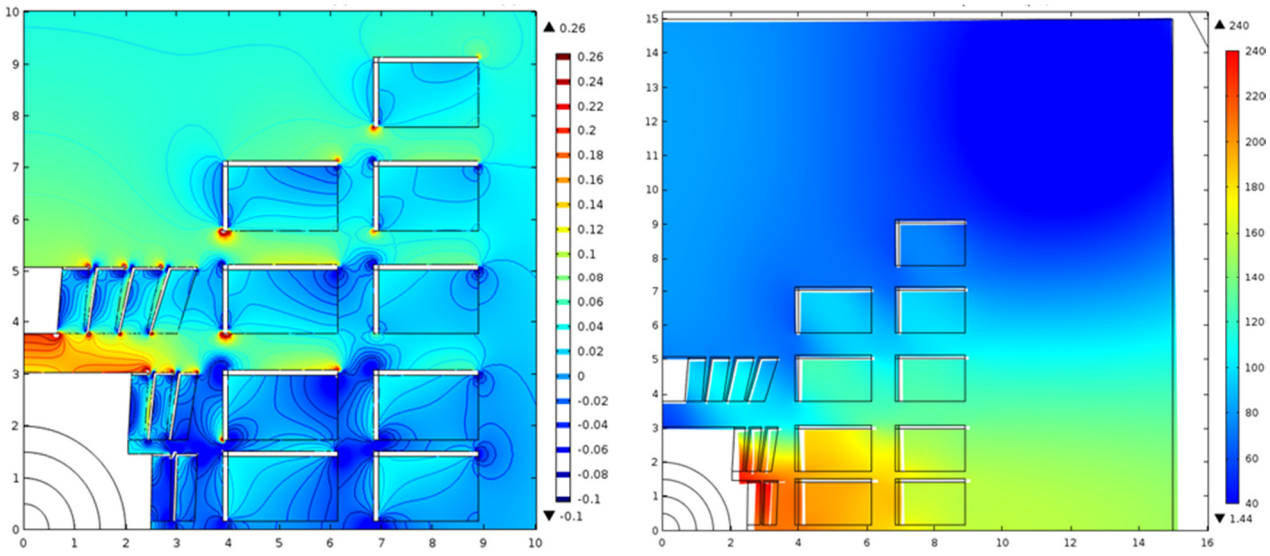

Fig. 47a&b. Volumetric strain ε [%] and deformation δ [μm] in magnet of Figs. 45-46a. Left: In the horizontal web inboard of the most-outboard set of HTS windings the average ε at $x = 0$ is ~0.21%. Right: δ, amplified tenfold; δ_{max} is a 240-μm rightward displacement of the most-inboard HTS winding block.

Objective 4: Coil Ends (practice windings)

This task was carried out jointly by BNL and e2P, conferring with PBL. Short coils of the two types of lifted ends were built (one at BNL and another at e2P) and tested at 77 K.

Model coil winding tests at BNL

This STTR wound tape coils having novel geometries, especially ones compatible with the 2-in-1 common coil geometry. To develop winding techniques in which HTS tapes are aligned favorably with the field, BNL wound several practice coils of up to 200 turns of stainless steel tape. The coil was first wound flat, followed by twisting the ends or straight sections to the desired orientation. When the winding depth exceeded several mm, end spacers were needed to reduce strain on the conductor. To avoid excessive strain and to allow the ends to take their natural shape, the end blocks were lifted a few centimeters (see Fig. 48). In some magnets this is acceptable, but not for tests in the BNL common-coil dipole, in which the test opening is only 30 mm across. Several trials were made (see Fig. 49) to satisfy this constraint, but the eventual tests used racetrack coils.

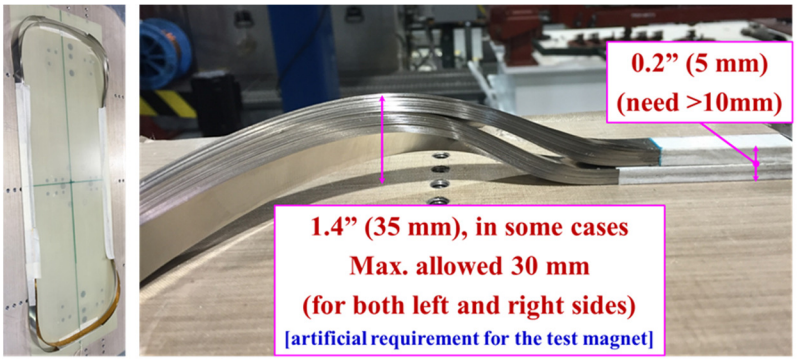

Fig. 48. Practice winding of 12- and 100-turn coils of stainless steel tape.

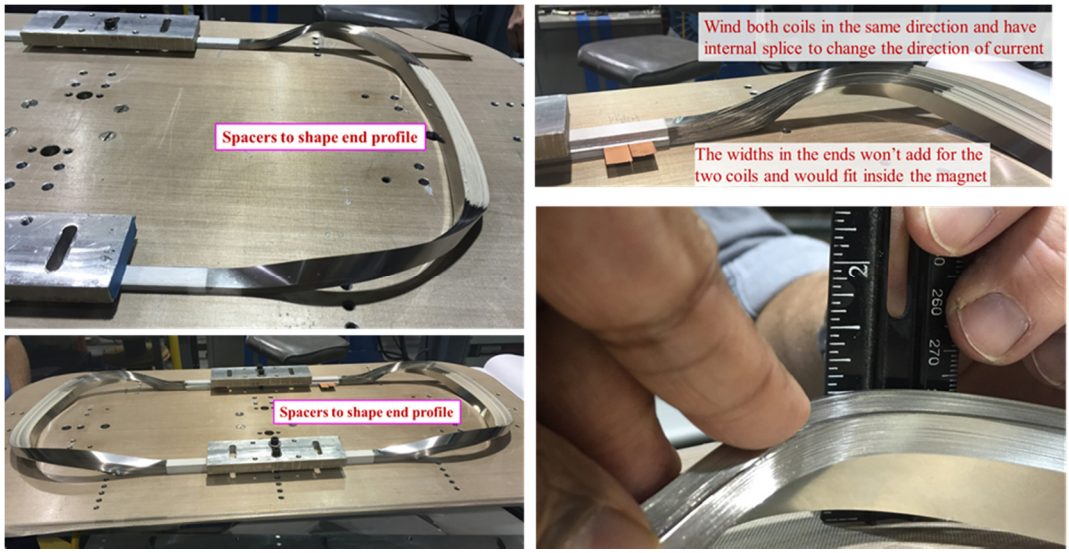

Fig. 49. Attempts to reduce strain, and lifting of the end block in 200-turn coil of stainless steel tape.

Model coil winding tests at e2P

The first coil fabricated at e2P was a racetrack coil with semicircular ends and straight sections rotated so that the c-axis of the tape was parallel to the axis of the ends of the coil. The coil had three turns of Hastelloy ribbon 12 mm wide by 0.10 mm thick. The coil was easy to wind and had a very low profile; however, where the tape was twisted to transition from circular end to straight section the tape buckled across its width; this creasing/buckling could degrade the critical current of the conductor by straining it excessively.

To address this issue e2P developed a second method for winding dipole coils, refining the winding former and winding technique for the second iteration of the square-end coil. e2P wound a coil using SuNam 2nd-generation (2G) High Temperature Superconducting (HTS) tape with architecture as in Fig. 50a. The tape was insulated (spiral wrap) with Kapton, with no apparent degradation in performance, as per the 77 K test results shown in Fig. 50b.

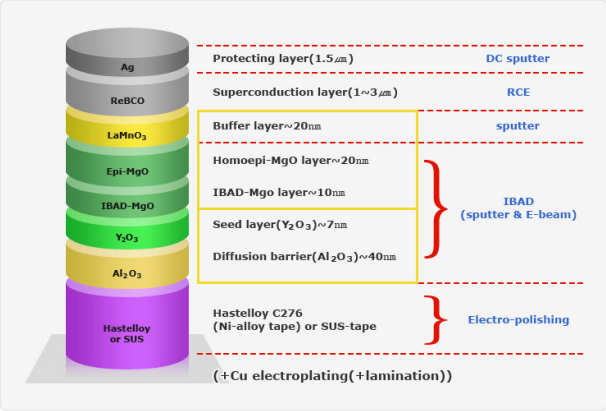

Fig. 50a. Architecture of SuNam 2G Tape[2] wound by e2P.

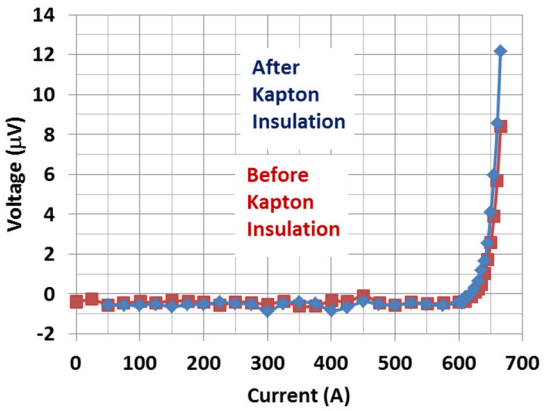

Fig. 50b. V vs. I of SuNam tape tested at 77 K.

This coil design achieves a low-profile overpass via "square" corners in which the tape inverts as it negotiates each corner, as shown in Fig. 51. The finished coil is 10 turns, wet wound with Stycast 2850 FT blue epoxy, of SuNam 2G HTS tape with Kapton insulation spiral wrap. Table II summarizes its dimensions.

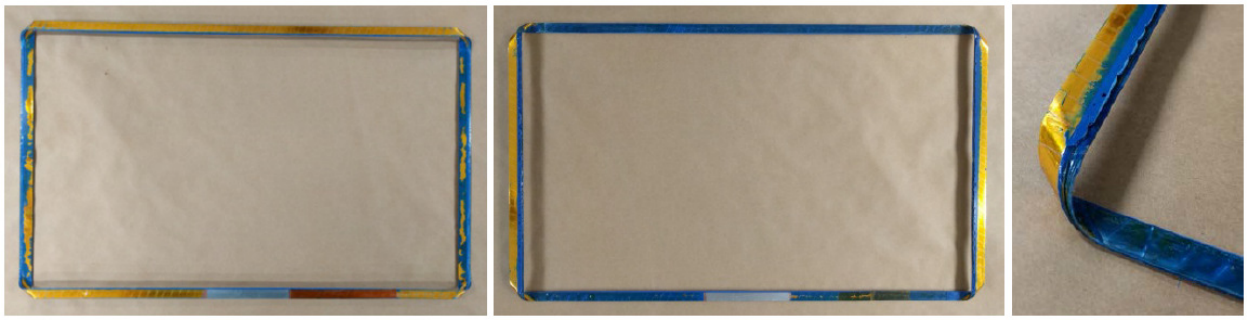

Fig. 51. Ten-turn Square Coil wound at e2P with Kapton-insulated SuNam 2G HTS tape and Stycast 2850FT blue epoxy[3].

Table II. Dimensions of e2P Square Coil[3]

Coil Parameter	Dimension (mm)
Height of single coil at end turn	17
Overall Width of coil	384
Overall coil length	644
Coil straight section length	584
Thickness of the straight section	2.89

e2P tested the coil in liquid nitrogen (LN_2) to determine its self-field critical current and *n* value. Figure 52a&b shows the LN_2 test setup and the critical current test result.

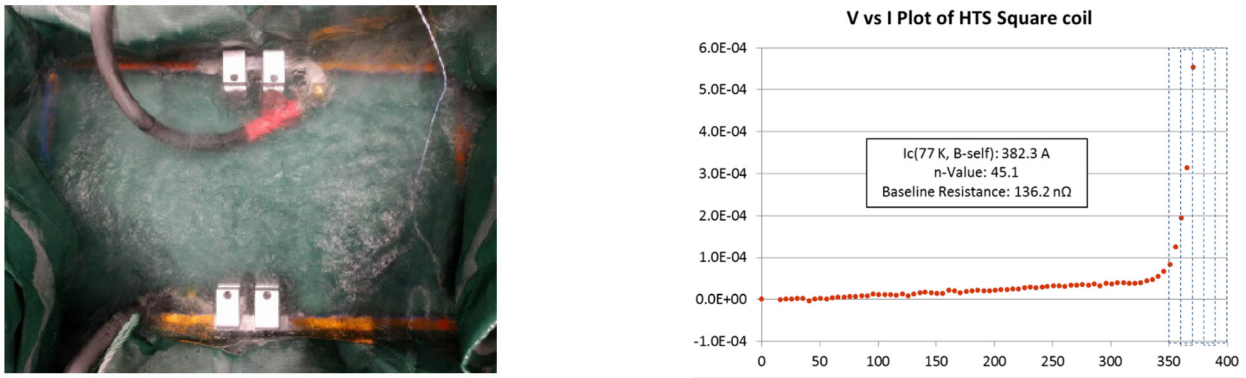

Fig. 52a&b. Left: LN_2 I_c testing of Square Coil by e2P[3]. Right: I_c and *n* value of SuNam 2G HTS tape at 77 K.

Square-coil tests at BNL

BNL performed further tests on the Square Coil to confirm its performance, search for conductor degradation at its square ends, and diagnose the linear voltage increase from zero to 350 A seen in Fig. 52b; suspected was non-superconductivity of the lead connection. Superconducting leads were installed, and then additional voltage-taps were soldered to the beginning and end of each corner of the first turn of the coil after removing some Kapton insulation. Due to the epoxy bonding of the coil, only the first turn of the coil was accessible for voltage-tap placement.

BNL Test Setup

As shown in Fig. 53a, BNL mounted the e2P Square Coil on a Micarta board for LN_2 testing. Voltage taps were indium soldered at the beginning and end of each corner of the first turn to monitor the corner performance through the critical current test, as shown in Figure 53b. Strips of Superpower 2G HTS tape (with similar architecture and performance to SuNam 2G HTS conductor) were soldered onto copper leads for positive and negative terminal connections to the Square Coil. The Superpower 2G HTS conductor was soldered directly onto the Square Coil to make a nearly-superconducting lead connection. Additional voltage taps were soldered before and after the lead connections to gauge their performance. The leads were then connected to a Hewlett Packard 6680A DC Power Supply System (Max Voltage: 3.3V; Max Current: 1 kA). Figure 54 shows the coil configuration and experimental setup.

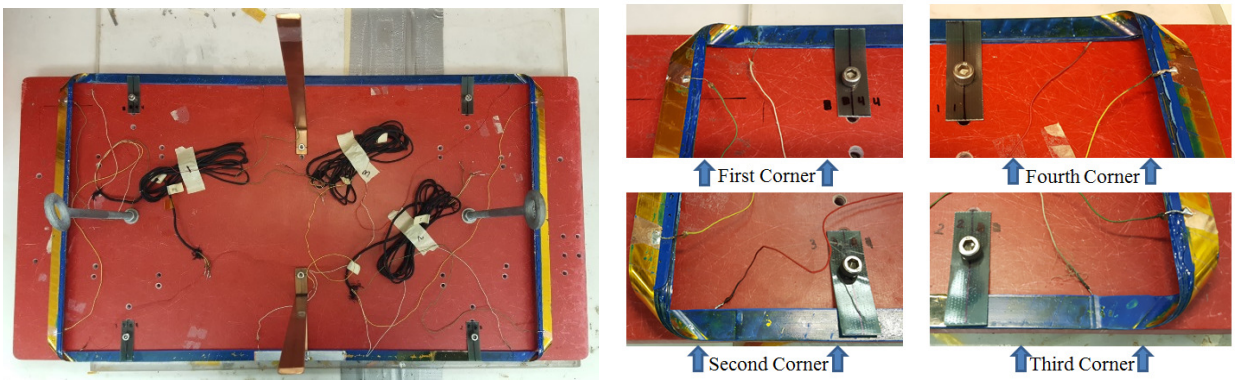

Fig. 53a&b. Left: e2P Square Coil fitted to a modified Micarta board for LN_2 testing. Right: Voltage taps in all four corners of the first turn.

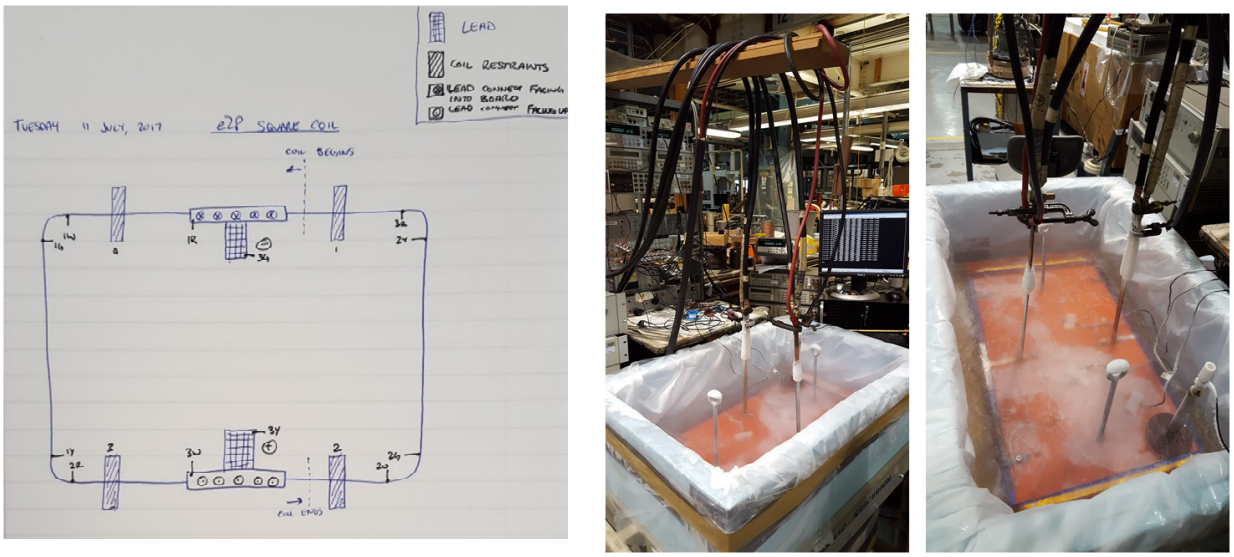

Fig. 54a-c. Left: Square Coil setup configuration. Center: Foam container for LN_2 and Square Coil. Right: Square Coil in LN_2 bath with data acquisition system in the background.

Test Procedure

In a foam "bathtub" being filled with liquid nitrogen, the Square Coil carried 1 A until it went superconducting, zeroing all voltages. Current was ramped up in increments of 10, 25, or 50 A during multiple test runs to obtain comprehensive data. After 325 A, the increments were decreased to 2-5 A. Each data point had either ten or a hundred line cycles (L.C). To reduce noise, a bypass was added to the positive lead in test runs 2 to 4; extra connections from the power-supply were added from Test Run 3 onwards.

Test Results

In Run 1, with only ten line cycles per data point, the negative and positive leads showed the greatest voltage/resistance of all the components being tested. In all five runs, voltage runaway was very consistent: 376.2 A, 376.4 A, 376.3 A, and 378.1 Typically the first and third straights

showed resistive voltage beyond 350 A, whereas the corners behaved well. In Run 3 extra connections from the power-supply and an increase from 10 to 100 line cycles markedly improved the noise level relative to the previous runs. An extra data-set—the performance of the whole coil minus the leads—was acquired for this and following runs. For representative data of voltage versus current, see Figure 55a for the entire coil, and 55b for the first turn.

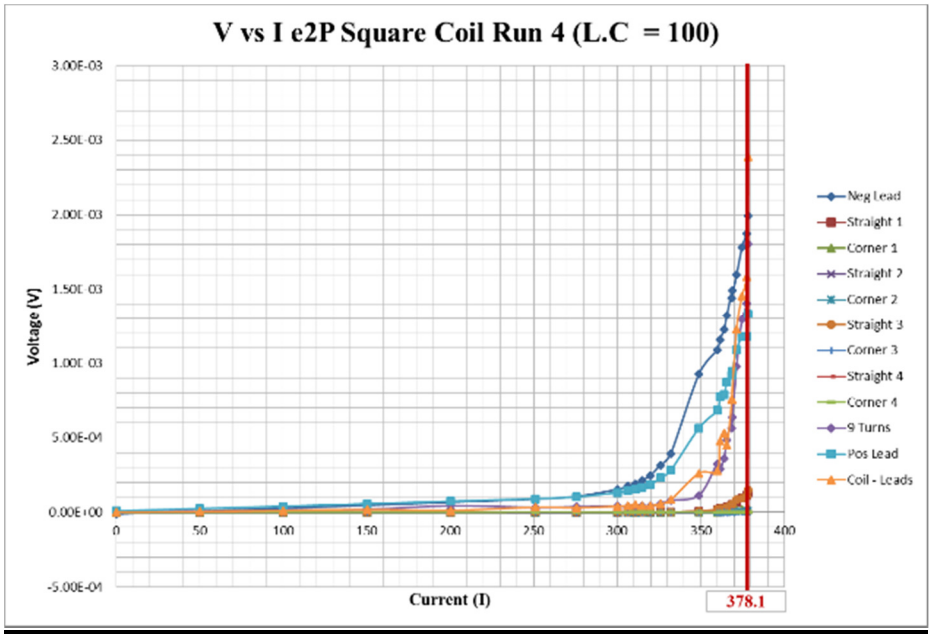

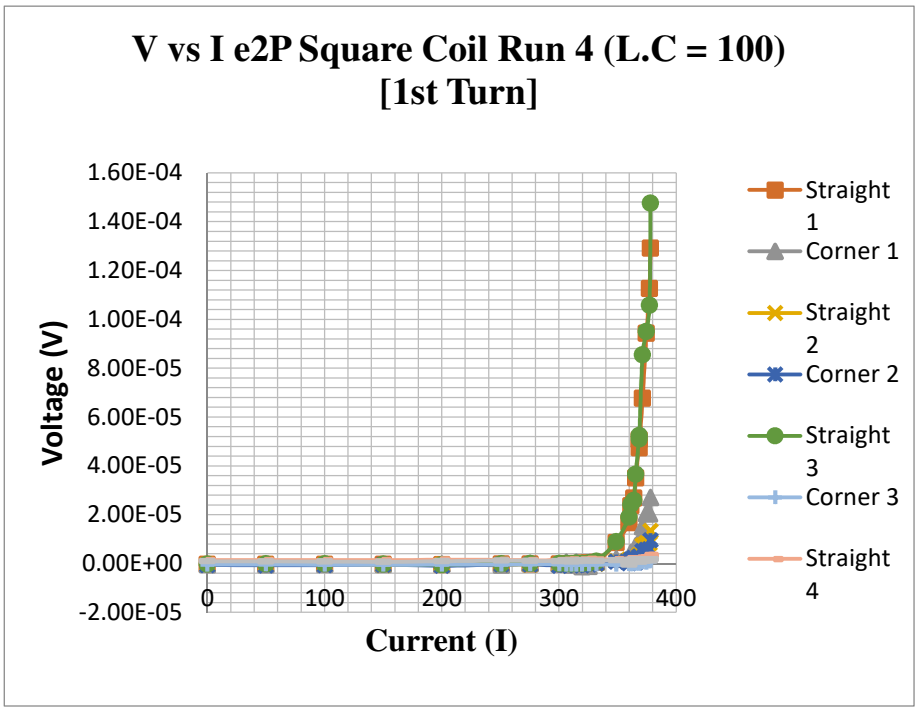

Fig. 55a&b: Voltage vs. current during fourth test run of Square Coil. Top: Entire coil. Bottom: First turn.

Figure 56a shows data from the fifth test run, whose purpose was earlier detection of the onset of resistivity. At 350 A the power supply was shut off and allowed to cool, resulting in a minor dip in voltage from the increase in performance from the cooling of the coil along with the power supply. Figure 56b computes the *n* value to be 38.7, excellently high.

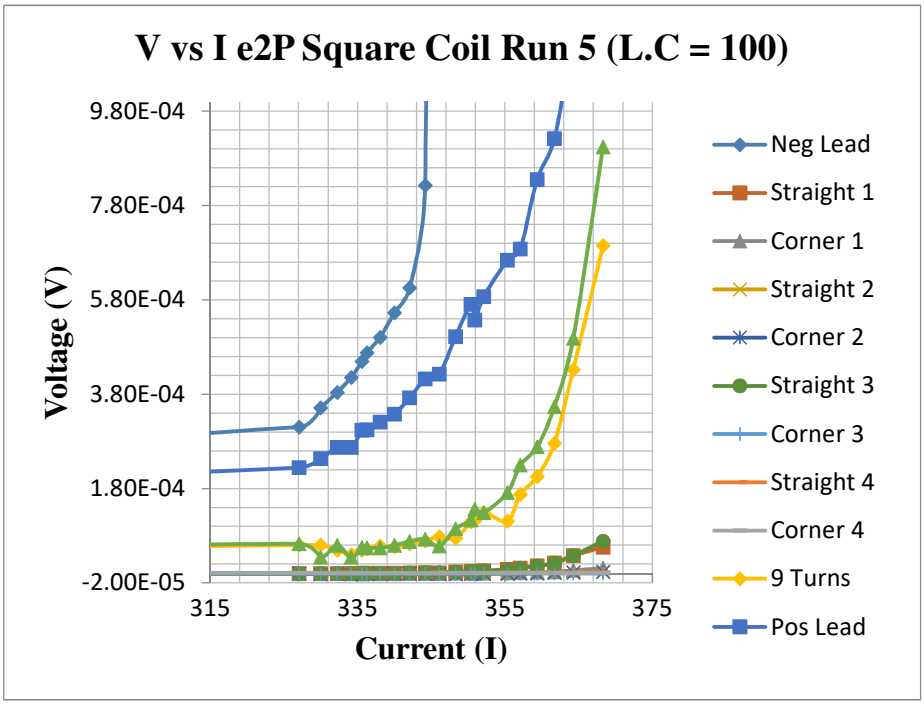

n-Value

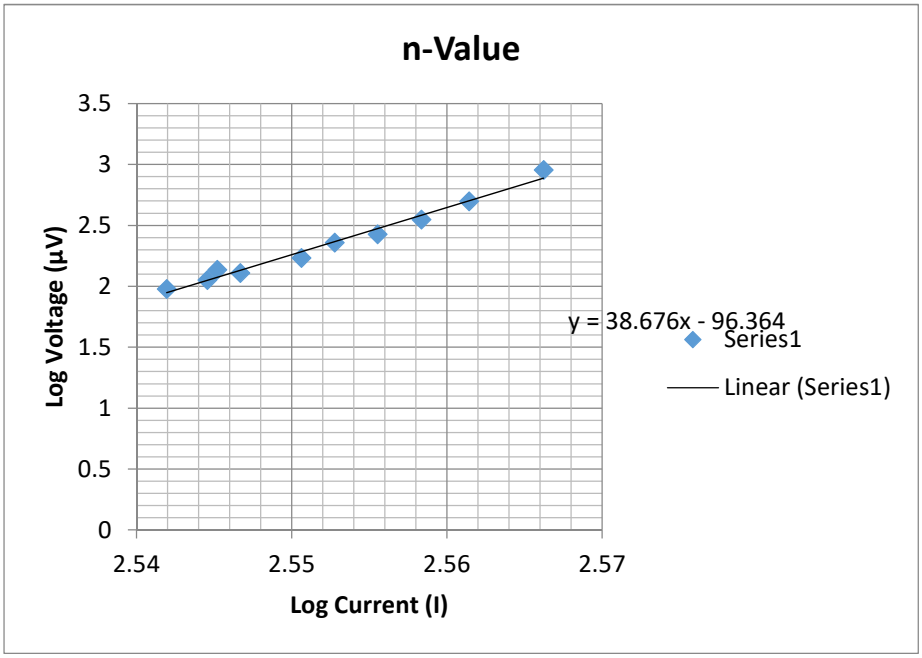

Fig. 56a&b. Top: Overall data from the fourth test run of the Square Coil. Bottom: *n* value of Square Coil.

Discussion

The Square Coil was wound using 20 m of SuNam 2G HTS tape. The industry standard for critical current is 1 μV/cm; for the Square Coil it will be reached at 2 mV. Data analyzed from Test Run 4 (Fig. 55) gives the Square Coil's critical current at 378.1 amps. The *n* value was calculated to be 38.7 (Fig. 56), signifying good conductor behavior. Superconducting leads eliminated the resistance below 350 A that was observed in the e2P test, implicating their non-superconductor-to-superconductor lead connection. All four corners of the first turn showed no conspicuous signs of conductor performance degradation from the corner bends. The 1st and 3rd straights of the first turn showed an onset of resistive voltage near 350 A.

Objective 5: Cost Reduction

In addition to demonstrating technology for high field HTS/LTS hybrid magnets was a goal to reduce the cost of high field magnets. Orienting tape parallel to the field should reduce the amount of expensive HTS needed for a given field, because its current carrying capacity becomes several times higher. The common-coil design should reduce cost because the racetrack coil geometry adequate for most coils is simpler, and because half as many coils suffice, each coil serving both apertures. An additional potential cost saver is that the common-coil geometry accommodates "react & wind" technology (as used in DCC017), and therefore is not constrained to a limited number of insulating materials and manufacturing processes.

Objective 6: Commercialization and Technology Transfer to e2P

PBL teamed up with Energy to Power Solutions (e2P) and Brookhaven National Laboratory (BNL) to promote bringing to the marketplace the HTS technology developed during this STTR. PBL has developed significant IP and has a team of technology, managerial and legal experts who have worked with industries in building superconducting magnets. PBL, however, does not have its own cryo-testing and manufacturing facilities. e2P is a small private company with its own infrastructure, facilities and revenues and has a significant program of its own on HTS magnets. In addition to manufacturing and testing HTS coils, e2P's collaboration with PBL and BNL was a vital part of the planned technology transfer. HTS technology is of great interest not only for accelerator magnets but also for high field NMR, medical gantries and wind turbines.

PBL and its partner BNL shared with e2P key technical aspects of the HTS coil design that allowed it to build some of the HTS coils for the HTS/LTS hybrid magnet. e2P participated in monthly teleconferences and the onsite annual team meeting. PBL shared the design and technology and allowed and encouraged e2P to design and develop a new coil concept with conductor provided by the PBL/BNL team after insulating it with helically wrapped Kapton. e2P tested that coil onsite and then sent it to BNL for further testing. e2P purportedly is using in other projects the novel coil design developed through this STTR, exemplifying commercialization of the design and technology developed under this STTR program.

CONSULTANTS AND SUBCONTRACTORS (INCLUDING RESEARCH INSTITUTION)

No consultants were involved with this STTR; BNL and e2P were subcontractors. Brookhaven National Laboratory, 30 Bell Ave., Bldg. 460, Upton, NY 11973 is the research institution on this work. BNL played a major role in the Phase II effort, as is described throughout this proposal and indicated by the budget.

PBL is pleased to partner with BNL and use the considerable BNL facilities in the Phase II work.

SUMMARY AND IMPACT

Successful operation of the HTS coils with Nb_3Sn coils demonstrates the practicality of HTS/LTS hybrid dipoles. The HTS coils remained protected during operation and showed no measurable degradation despite half a dozen quenches. Magnetic measurements indicate that the magnetization effects are strongly dependent on the coil geometry and might be kept low enough for accelerator magnets if the HTS tape is aligned closely parallel to the ambient field. Facilitating the STTR was a BNL common-coil magnet of unique design and structure with a large opening in which to insert HTS coils for testing without the prohibitive cost in time and money to disassemble and reassemble the magnet.

Successful demonstration of high field magnets using our proposed technique can have a major impact in the field of accelerator magnets. High strength ReBCO conductors with a Hastelloy substrate have always been preferred in high field magnets, because of their high strength and therefore ability to withstand large stresses, but they were seen as impractical, primarily because of the likelihood of large field errors arising from the conductor magnetization of the tape geometry. The technique developed during the course of this work addressed that shortcoming. As a result, very high field magnets made with ReBCO HTS tape may now become viable for future circular colliliders. The design techniques developed here may reduce markedly the quantity and hence the cost of expensive HTS. The team developed a preliminary design of a high field magnet with a goal of easy manufacturability and reduced cost in a large-volume industrial production.

REFERENCES

1. "Building for Discovery: Strategic Plan for U.S. Particle Physics in the Global Context," P5 Report, http://science.energy.gov/~/media/hep/hepap/pdf/May%202014/FINAL_P5_Report_053014.pdf
2. Future Circular Collider Study Kickoff Meeting, Geneva, Feb. 12-14, 2014, http://indico.cern.ch/event/282344/timetable/#20140212
3. CEPC/SppC study in China, http://indico.cern.ch/event/282344/session/1/contribution/65/material/slides/1.pdf
4. R. Gupta, et al., "React & Wind Nb_3Sn Common Coil Dipole," ASC 2006, Seattle, WA, USA Aug. 27-Sept. 1, 2006.
5. R. Gupta, et al., "Recent Results in High Field HTS Magnet Technology," 2014 Kyoto Workshop on HTS Magnet Technology for High Energy Physics, Nov. 13-14, 2014, https://indico.cern.ch/event/319762/session/6/contribution/12/material/slides/0.pdf
6. J. van Nugteren, et al., "Study of a 5 T Research Dipole Insert Magnet using an Anisotropic ReBCO Roebel Cable," IEEE Trans. Appl. Supercond., 15 Oct., 2014.
7. Case Number: BNL15-02 for invention disclosure at Brookhaven National Laboratory on "Reduction of magnetization-induced field errors in High Temperature Superconductor (HTS) magnets by aligning the tape axis with magnetic field lines," Nov., 2014.
8. R. Gupta, et al., "Hybrid High Field Cosine Theta Accelerator Magnets with Second Generation HTS," ASC 2014, Charlotte, NC, USA, Aug. 10-15, 2014.
9. R. Gupta, et al., "High Field HTS Solenoid for a Muon Collider – Demonstrations, Challenges and Strategies," Int. Conf. on Magnet Tech., MT23, Boston, USA, July 2013.
10. P. Joshi, et al., "Novel Quench Detection System for HTS Coils," 2011 Particle Acc. Conf., New York, NY, May 2011.
11. H. Witte, et al., "Reduction of the Hot Spot Temperature in HTS Coils," Int. Conf. on Magnet Tech., MT23, Boston, USA, July 2013.
12. P.D. Noyes, et al., "Protection Heater Development for REBCO Coils," IEEE Trans. on Appl. Supercond., Vol. 22, Issue 3, 4704204 (2012).
13. R.C. Gupta, "A Common Coil Design for High Field 2-in-1 Accelerator Magnets," 1997 Particle Acc. Conf., Vancouver, Canada (1997).
14. J. Cozzolino, et al., "Magnet Engineering and Test Results of the High Field Magnet R&D Program at BNL," Appl. Supercond. Conf., Houston, TX, USA (2002).
15. R. Gupta, et al., "Status of High Temperature Superconductor Magnet R&D at BNL," Int. Conf. on Magnet Tech. (MT-18), Morioka City, Japan (2003).
16. R. Gupta, et al., Field Quality Optimization in a Common Coil Magnet Design, Int. Conf. on Magnet Tech. (MT-16), Ponte Vedra Beach, Florida, USA (1999).
17. R. Gupta, et al., "HTS Quadrupole for FRIB - Design, Construction and Test Results," ASC 2014, Charlotte, NC, USA, Aug. 10-15, 2014.
18. W.B. Sampson, "Superconducting Magnets for Beam Handling and Accelerators", pp. 574-578, Proc. of the Second Int. Conf. on Magnet Tech., Oxford, 1967.
19. R. Gupta, "HTS Open Midplane Dipole," 2008 Low Temperature Superconductor Workshop, Tallahassee, FL, Nov. 11-13, 2008. http://www.bnl.gov/magnets/staff/gupta/Talks/ltsw08/ltsw08-omd-gupta.pdf
20. G. Sabbi, et al., "Performance characteristics of Nb_3Sn block-coil dipoles for a 100 TeV hadron collider," ASC 2014, Charlotte, NC, USA, Aug. 10-15, 2014.

21. R. Blackburn, et al., "Fabrication of TAMU3, a wind/react stress-managed 14T Nb_3Sn block coil dipole," 8th Eur. Conf. on Appl. Supercond. EUCAS'07 (2008).
22. BNL's Magnet Program Vision for HEP Colliders, DOE GARD magnet workshop, Washington, DC, July 28, 2015. https://www.bnl.gov/magnets/Staff/Gupta/Talks/GARD2015/bnl-gard-july-2015-gupta1.pdf
23. Protection Experience and HTS Magnets at BNL, 3rd Workshop on Accelerator Magnets in HTS (WAMHTS-3), Lyon, France, Sept. 11, 2015. https://www.bnl.gov/magnets/Staff/Gupta/Talks/WAMHTS-3/wamhts-3-gupta-rev.pdf
24. Common Coil Magnet Design for High Energy Colliders, Seminar at CERN, Sept. 15, 2015. https://www.bnl.gov/magnets/Staff/Gupta/Talks/cern-cc-seminar-2016/cern-seminar-gupta-2015.pdf
25. L. Bottura, et al. "Advanced Accelerator Magnets for Upgrading the LHC," IEEE/CSC & ESAS European Supercond. News Forum, No. 19. IEEE Trans. Appl. Supercond. 22, (4002008) (2012).
26. CEPC-SppC Preliminary Conceptual Design Report, Vol. II: Accelerator. http://cepc.ihep.ac.cn/preCDR/Pre-CDR_final_20150317.pdf .
27. R. Gupta, et al., "React & Wind Nb_3Sn Common Coil Dipole," IEEE Trans. Appl. Supercond., Vol. 17, No. 2, (2007), pp 1130-1135.
28. R. Gupta, "A common coil design for high field 2-in-1 accelerator magnets," Particle Acc. Conf., Vancouver, BC, pp. 3344-3346 vol.3, 1997.
29. R. Gupta, "HTS/LTS Hybrid Test Results and Common Coil Design Update," FCC Week 2017, Berlin, Germany, May 29 - June 2, 2017. https://indico.cern.ch/event/556692/
30. R. Gupta, "Hybrid Configuration and BNL Activities," US MDP 1st General Meeting & Workshop Napa Valley, CA, Feb. 6-8, 2017. https://conferences.lbl.gov/event/73/
31. R. Gupta, "ReBCO at BNL," 4th Workshop of the series Accelerator Magnets in High Temperature Superconductors (WAMHTS-4), Barcelona, Spain, Feb. 15-17, 2017. https://indico.cern.ch/event/588810/
32. P.N. Joshi, et al., "LTS-HTS Hybrid Dipole Magnet Quench Protection System," 25th Int. Conf. on Magnet Tech., Amsterdam, the Netherlands, 2017, Paper Thu-Mo-Or28-03.
33. R. Gupta, M. Anerella, J. Cozzolino, P. Joshi, W. Sampson, P. Wanderer, J. Kolonko, D. Larson, R. Scanlan, R. Weggel and E. Willen, "Design, Construction and Test of HTS/LTS Hybrid Dipole," 25th Int. Conf. on Magnet Tech., Amsterdam, the Netherlands, 2017.

SECTION TWO, PART ONE – PUBLICATIONS AND PATENTS GRANTED

The Phase II effort resulted in the granting of a patent:

> US Patent number 9793036: "A Low Temperature Superconductor and Aligned High Temperature Superconductor Magnetic Dipole System and Method for Producing High Magnetic Fields".

The Phase II effort also resulted in the following publication:

> R. Gupta, M. Anerella, J. Cozzolino, P. Joshi, W. Sampson, P. Wanderer, J. Kolonko, D. Larson, R. Scanlan, R. Weggel and E. Willen, "Design, Construction and Test of HTS/LTS Hybrid Dipole," presented at the 25th Int. Conf. on Magnet Technology, Amsterdam, the Netherlands, 2017.

In addition, the Phase II effort also resulted in the following presentations:

1. BNL's Magnet Program Vision for HEP Colliders, DOE GARD magnet workshop, Washington, DC, July 28, 2015. https://www.bnl.gov/magnets/Staff/Gupta/Talks/GARD2015/bnl-gard-july-2015-gupta1.pdf
2. Protection Experience and HTS Magnets at BNL, 3rd Workshop on Accelerator Magnets in HTS (WAMHTS-3), Lyon, France, Sept. 11, 2015. https://www.bnl.gov/magnets/Staff/Gupta/Talks/WAMHTS-3/wamhts-3-gupta-rev.pdf
3. Common Coil Magnet Design for High Energy Colliders, Seminar at CERN, Sept. 15, 2015. https://www.bnl.gov/magnets/Staff/Gupta/Talks/cern-cc-seminar-2016/cern-seminar-gupta-2015.pdf
4. R. Gupta, "HTS/LTS Hybrid Test Results and Common Coil Design Update," FCC Week 2017, Berlin, Germany, May 29 - June 2, 2017. https://indico.cern.ch/event/556692/
5. R. Gupta, "Hybrid Configuration and BNL Activities," US MDP 1st General Meeting & Workshop Napa Valley, CA, Feb. 6-8, 2017. https://conferences.lbl.gov/event/73/
6. R. Gupta, "ReBCO at BNL," 4th Workshop of the series Accelerator Magnets in High Temperature Superconductors (WAMHTS-4), Barcelona, Spain, Feb. 15-17, 2017. https://indico.cern.ch/event/588810/
7. P.N. Joshi, et al., "LTS-HTS Hybrid Dipole Magnet Quench Protection System," 25th Int. Conf. on Magnet Tech., Amsterdam, the Netherlands, 2017, Paper Thu-Mo-Or28-03.
8. R. Gupta, M. Anerella, J. Cozzolino, P. Joshi, W. Sampson, P. Wanderer, J. Kolonko, D. Larson, R. Scanlan, R. Weggel and E. Willen, "Design, Construction and Test of HTS/LTS Hybrid Dipole," 25th Int. Conf. on Magnet Tech., Amsterdam, the Netherlands, 2017.